Journal of Volcanology and Geothermal Research 472 (2026) 108566

Contents lists available at ScienceDirect

Journal of Volcanology and Geothermal Research

journal homepage: www.journals.elsevier.com/journal-of-volcanology-and-geothermal-research

From alteration to avalanche: A 3D framework for exploring hydrothermal weakening of lava domes

K.D. Ní Nualláin [a,*], C.E. Harnett [a,b], A. Hrysiewicz [a,b], M.J. Heap [c], T.R. Walter [d], M. Rosas-Carbajal [e]

[a] UCD School of Earth Sciences, University College Dublin, Dublin, Ireland
[b] Research Ireland Centre for Applied Geosciences (iCRAG), University College Dublin, Dublin, Ireland
[c] Université de Strasbourg, CNRS, Institut Terre et Environnement de Strasbourg, Strasbourg, France
[d] GFZ German Research Centre for Geosciences, Potsdam, Germany
[e] IRFU, CEA, Université Paris-Saclay, Gif-sur-Yvette F-91191, France

ARTICLE INFO

Keywords:
Lava dome
Hydrothermal alteration
Collapse
Discrete element method
Debris avalanche
Slope Stability

ABSTRACT

Volcanic domes are inherently unstable structures that form when lava is too viscous to flow away from the vent. Dome collapse poses a hazard via volcanic landslides and debris avalanches that can threaten nearby communities. Dome collapse can be promoted by hydrothermal alteration, which can weaken volcanic rock and is commonly concentrated in regions with high fluid flow, such as fractures and areas of high permeability within the dome. Here, we focus on understanding how alteration affects dome stability, collapse volumes and runout distances, using the case study of La Soufrière de Guadeloupe, in the Eastern Caribbean. We present new 3D models that combine geophysical and mechanical data to investigate different post-emplacement dome stability scenarios that incorporate hydrothermal alteration. Our results demonstrate that increased alteration-induced weakening (i.e., to 50% or 10% of the original rock strength) leads to greater displacements and causes dome destabilisation. Additionally, we show displacement and finite shear strain as a result of varying the spatial extent (the thickness and location) of the alteration zones. We also show that incorporating mechanical heterogeneity is crucial for accurate hazard modelling. We introduce a novel method using the La Soufrière de Guadeloupe dome to offer a comprehensive understanding of the alteration process from initiation to deposit. Our results indicate that hydrothermal alteration significantly increases collapse volumes and thus runout distances, which are critical for understanding the potential impact of dome collapse and a critical motivation for our 3D modelling approach. By capturing the full process from internal weakening to hazard potential, this method enhances our ability to anticipate future dome collapse events, and thus, mitigate their effects.

1. Introduction

Lava domes form when magma extrudes from the vent of a volcano and is too viscous to flow away; thus, it piles up around the vent (Calder et al., 2015). Domes are inherently unstable structures as they grow incrementally, with varied geometries (Myers et al., 2024), extrusion rates (Huppert et al., 1982; Husain et al., 2019), material properties (Harnett et al., 2019; Heap et al., 2023b; Kendrick et al., 2021; Poganj et al., 2025), velocities (Walter et al., 2019b), and directions of flow (Walter et al., 2022; Zorn et al., 2019). Volcanic dome instability can result in their collapse, which can trigger hazards, such as turbulent and hot debris avalanches, pyroclastic density currents, rock falls (Calder et al., 2002), lateral explosions, and explosive eruptions due to rapid magma depressurisation (Calder et al., 2015). Over the last 10,000 years, there have been over 20,000 recorded partial flank collapses at 200 volcanoes worldwide (Siebert et al., 2010). 22% of these collapses were associated with phreatic and/or hydrothermal activity (Siebert, 1984; Siebert et al., 2010, 1987). Significant recent events, such as the 2018 flank collapse of Anak Krakatau (Walter et al., 2019a), emphasise the continued relevance of these hazards. Further, 13% of dome-forming episodes are associated with major explosive activity (volcanic explosivity index, VEI $\geq$4) (Ogburn et al., 2015). Thus, management and mitigation of volcanic collapse hazards are crucial.

Previous studies have investigated specific causes of lava dome

* Corresponding author.
E-mail address: kendra.ninuallain@ucdconnect.ie (K.D. Ní Nualláin).

https://doi.org/10.1016/j.jvolgeores.2026.108566
Received 3 October 2025; Received in revised form 13 January 2026; Accepted 11 February 2026
Available online 16 February 2026

collapse (Harnett, 2019; Sheldrake et al., 2016). Lava domes can be destabilised via gravitational collapse (Ui et al., 1999), oversteepening due to extrusion (Ashwell et al., 2018; Diefenbach et al., 2013), changes in extrusion rate (Vallance et al., 2008), gas overpressure (Voight and Elsworth, 2000), rainfall infiltration and interaction (Carn et al., 2004; Matthews et al., 2002; Matthews and Barclay, 2004; Heap et al., 2023a), morphological evolution (Hutchison et al., 2013), material property heterogeneity (Heap et al., 2023b), seismic swarms (Calder et al., 2002), and hydrothermal alteration (Reid, 2004). In this paper, we focus on post-emplacement dome stability, collapse volumes, and runout distances, particularly considering the effects of hydrothermal alteration.

Hydrothermal alteration is caused by the circulation of hot fluids within the Earth's subsurface (Pirajno, 2009). Hydrothermal fluids may originate as meteoric water, sea water, be derived from an exsolution of magma (Y. Zhang et al., 2023), or be a mixture of all three. Numerical, geophysical and geochemical investigations have shown that hydrothermal alteration can promote instability by either strengthening (Heap et al., 2021a) or weakening (Heap et al., 2021b) volcanic rock. Strengthening can occur when precipitated minerals reduce porosity and fill in pores and cracks (Heap et al., 2021a). However, this can also reduce permeability and inhibit fluid circulation (Mordensky et al., 2018; Heap et al., 2021a), thus increasing pore fluid pressurisation and increasing volcanic instability (Heap et al., 2021a; Reid, 2004). Alteration can also reduce rock strength, Young's modulus, cohesion and shear strength and produce weak, “rotten”, clay-rich rocks (del Potro and Hürlimann, 2009; Heap et al., 2021b). For example, laboratory studies have shown that hydrothermal alteration can reduce the uniaxial compressive strength (UCS) of andesite up to a factor of 10 (Darmawan et al., 2022).

Alteration has therefore been shown to weaken a volcanic edifice on a large scale, which can lead to collapse (Ball et al., 2015, 2013; de van Vries et al., 2000; del Potro and Hürlimann, 2009; Finn et al., 2018; Heap et al., 2021b; John et al., 2008; Reid et al., 2001; Rosas-Carbajal et al., 2016; Wallace et al., 2022; Zimbelman et al., 2004). Indeed, hydrothermally altered materials are seen in debris avalanche deposits at volcanoes worldwide, such as in Merapi (Indonesia), where alteration is thought to reduce rock strength and increase susceptibility to collapse when working in conjunction with external triggers (Darmawan et al., 2022). Geochemical and mineralogical analyses, along with remote sensing, showed a buried horseshoe-shaped zone defined by mechanically weak hydrothermally altered materials that lay beneath more recently extruded lava at Merapi, and ground monitoring techniques showed that the new lava dome was collapsing along this alteration zone (Darmawan et al., 2022). Thus, it is crucial to gain a better understanding of dome structure and subsurface alteration zones to identify the regions that are most unstable, and moreover, those most susceptible to collapse. Based on observations at Merapi and similar observations at frequently collapsing volcanoes worldwide, alteration is widely considered as a mechanism that causes edifice collapse and destructive debris avalanches.

Volcanic debris avalanches are large granular landslides, with typically long runout distances. For example, a study that modelled debris avalanches caused by hydrothermal alteration of Mount Ruapehu, New Zealand, suggested high susceptibility to collapse of the west and southwest flanks (Kereszturi et al., 2021). These authors found that resultant debris avalanches could exhibit runout distances of 20,000 m. The height-to-length ratios of channelised debris avalanches are significantly lower (i.e., longer runouts) than non-volcanic and unconfined subaerial landslides (Tost et al., 2014). Gravitational loading, loose soil, and elevated pore pressure (often due to groundwater oversaturation) in tandem with alteration processes, are among the triggers. In wet, tropical climates, such as at La Soufrière de Guadeloupe in the Eastern Caribbean, there is a higher risk of these hazards because of more prominent high pore-water content and geomorphic conditions (Ball et al., 2013). The presence of clays in rocks has been linked to changes in the rheological behaviour of debris flows, such as a decrease in effective viscosity (Bardou et al., 2007, 2004). Hydrothermal alteration leads to the formation of such clays and thus can affect the dynamics of a debris avalanche. For example, the formation of smectite clays in hydrothermally altered bedrock at Casita volcano, Nicaragua, reduced the shear strength of the rock and inhibited water infiltration (Opfergelt et al., 2006). Thus, the resulting weaker, clay-rich rock and increased pore pressure in the overlying rock (due to clogging) may have led to longer runout distances, and moreover, increased the hazard of the 1998 debris flow (Opfergelt et al., 2006).

Numerical models are essential for understanding volcanic slope instability. Previous studies numerically model volcanic slope instability by various methods, such as the finite element method (FEM) (Bourgouin et al., 2007; Hale, 2008; Hale et al., 2009a, 2009b; Hale and Wadge, 2008), the discrete element method (DEM) (Harnett et al., 2020, 2018; Harnett and Heap, 2021; Heap et al., 2023a, 2023b, 2021b), the finite difference method (Alvarez-Fernandez et al., 2013; He et al., 2008), the element-free method (Gago et al., 2019), the numerical manifold method (Yu et al., 2023), the boundary element method (Jiang and Zimmermann, 1992), and discontinuous deformation analysis (MacLaughlin et al., 2001). Here, we employ the DEM, as this approach contrasts with other modelling techniques that impose fracture patterns a priori and is particularly suited to capturing the brittle failure, emergent fracture networks, and block-scale deformation typical of volcanic dome collapse (Harnett et al., 2019, 2018) – processes that are difficult to simulate using continuum methods like FEM.

To date, models of volcanic instability using numerical simulations, such as the DEM and FEM, have largely focussed on 2D modelling. For example, Harnett and Heap (2021) developed 2D homogeneous models of lava dome stability using the DEM, where they reduced rock strength to simulate the effects of alteration. These authors found that a reduction in rock strength increased the volume of unstable material. 2D modelling, however, is a simplification of the 3D reality. Due to limited degrees of freedom, it cannot capture out-of-plane behaviour, such as bulging, arching, or redistribution of stress around weak zones (Wu et al., 2024; Zhang et al., 2015). Depending on the geometric assumptions (e.g., plane strain), 2D analysis may overestimate or underestimate stability compared to 3D; furthermore, it suffers from an absence of volume calculations and reduced geometric complexity. In addition, due to the lack of volume and depth information, it is not possible to determine the direction of collapse in a 2D model. Although more computationally expensive, 3D models can more appropriately consider the nature of a real-world system, especially one with topographic controls, as well as allow the calculation of collapse volumes. For example, a 3D FEM volcano flank model by Ball et al. (2018) showed that collapse volumes increase as a function of alteration-induced weakening, but that future studies should aim to constrain material property parameters, such as cohesion, to make better-informed estimates of collapse volumes.

An important factor in advancing models of volcanic instability is developing a more detailed understanding of the spatial variation in mechanical properties of volcanic rocks (Heap et al., 2021b; Poganj et al., 2025). Geophysical methods, particularly various tomography approaches, allow us to gain a better understanding of the subsurface (Barde-Cabusson et al., 2013; Cabrera-Pérez et al., 2024, 2023; Castro-Melgar et al., 2021; Darmawan et al., 2022; Lesparre et al., 2012; Miller et al., 2020; Rosas-Carbajal et al., 2017, 2016), and thus, physical rock properties, such as density variation. Recently, electrical resistivity tomography (measuring conductivity) has been combined with muon tomography (measuring density variation) at La Soufrière de Guadeloupe (Lesparre et al., 2012; Rosas-Carbajal et al., 2017). Muon tomography is a non-invasive imaging method that allows us to see inside 3D objects, such as volcanoes, by using cosmic ray particles called muons. The denser the material, the more muons are absorbed. Therefore, several muon detectors placed around the volcano collate multiple profiles to create a 3D image of the dome's interior. The muon data at La Soufrière de Guadeloupe revealed low-density anomalies in areas of high

conductivity that also corresponded to identified hydrothermal zones (Rosas-Carbajal et al., 2016). Full consideration of this subsurface heterogeneity is commonly under-represented in models despite its known effect on overall stability (Heap et al., 2023b). A recent study, which provided strength measurements for >500 variably altered andesites from La Soufrière de Guadeloupe, found that the volcanic dome is characterised by a pronounced strength heterogeneity (Poganj et al., 2025). The 2D DEM models presented in Heap et al. (2023b) demonstrated how the presence of diffuse heterogeneity (variations in material properties) within lava domes contributes significantly to dome instability. Heap et al. (2023b) concluded that collapse volumes of altered material may be even larger than previously estimated when diffuse heterogeneity is also considered.

In this study, we focus on the case study of La Soufrière de Guadeloupe, where at least 10 flank collapses have been identified in the last 15,000 years (Boudon et al., 2007; Komorowski, 2005). Evidence for the involvement of alteration in collapse is found in debris avalanche materials from the La Soufrière de Guadeloupe lava dome, as they are often comprised of altered rock (Salaün et al., 2011). Further, 2D models have highlighted that hydrothermal alteration could destabilise the southern flank of the dome at La Soufrière de Guadeloupe (Heap et al., 2021b). Here, we use new 3D DEM models to explore the influence of rock weakening as a result of hydrothermal alteration on the stability of La Soufrière de Guadeloupe, as well as collapse volumes and runout distances following instability and collapse. We have combined the morphology of the La Soufrière de Guadeloupe dome with rare petrophysical and geophysical data (Heap et al., 2021b; Rosas-Carbajal et al., 2017) to create novel and mechanically heterogeneous 3D DEM models.

One of our primary aims is modelling the link between alteration and collapse volumes to assess debris avalanche hazard potential. We model multiple scenarios that consider varied extents and spatial distribution of mechanical weakening as a result of alteration. We quantify alteration-induced displacement, and, for the first time, we perform 3D shear strain analysis of these DEM models to assess fracturing and dynamic failure, building on methods previously applied in 2D (e.g., Schöpfer et al., 2007; Holohan et al., 2015; Harnett et al., 2022). Further, we calculate collapse volumes for each modelled scenario. These volumes are integrated with debris avalanche modelling in VolcFlow (Kelfoun et al., 2009) to determine runout distances, thicknesses and potential hazard. Our objective is to understand how mechanical rock weakening due to alteration influences dome stability and contributes to potential collapse by linking internal weakening to the volume of material involved and the scale of resulting runout hazards.

2. Geological setting: La Soufrière de Guadeloupe

La Soufrière de Guadeloupe is an andesitic stratovolcano on the French island of Basse-Terre in theGuadeloupe archipelago (Eastern Caribbean). La Soufrière de Guadeloupe is the most recent volcanic edifice in the Grande Découverte volcanic complex, with known eruptions from circa 9000 years ago (Moretti et al., 2020). There have since been 15 magmatic eruptions (nine of which were lava dome eruptions) identified on La Soufrière de Guadeloupe (Peruzzetto et al., 2019). The last major magmatic eruption was in 1530 CE and formed the present-day dome of La Soufrière de Guadeloupe (Komorowski, 2005; Lesparre et al., 2012; Peruzzetto et al., 2019).

Boudon et al. (2007) documented flank stability in the Lesser Antilles Arc, including La Soufrière de Guadeloupe. These authors found that at least 13 collapse events have occurred at La Soufrière de Guadeloupe over the last 140,000 years. The three oldest debris avalanche deposits were discovered in the Rivière des Pères on the southwestern flank of the volcano, dated between 140 and 42 ka. Some debris avalanche deposits were also located to the east of the volcano, dated circa 46 ka (Boudon et al., 2007). The 10 identified flank collapses within the last 15,000 years were mostly on the southwest flank of the volcano. Some collapses occurred on the southern and eastern flanks, with debris flows reaching the Atlantic coast up to 10,000 m away. One collapse that did not involve any magma input occurred in 11,500 BP. This collapse was on the western flank and resulted in a 300×10^6 m^3 debris avalanche and the formation of the Carmichaël crater. During the last 7700 years, 8 flank collapses that produced substantial debris avalanches (Boudon et al., 2007; Friant et al., 2006; Komorowski, 2005; Peruzzetto et al., 2019) reached runout distances of 5,000–15,000 m. Boudon et al. (2007) found that small collapse volumes (20–50 $\times$ 10^6 m^3) from these flank collapses formed debris avalanches within 5,000 m of the vent, and once channelised and accumulated, reached up to 60 m in thickness. In addition, large-volume avalanches that overflowed the palaeoriver drainages and became non-channelised, were up to 10 m in thickness. Boudon et al. (2007) highlighted that the deposits discovered were mostly composed of hydrothermally altered material. In 3100 BP, a flank collapse on the southwestern flank followed by a lateral blast formed the Amic amphitheatre crater (Fig. 1b). In 1530 CE, a small flank collapse that reached the Caribbean Sea near Basse-Terre (10,000 m away) occurred before the eruption and magmatic events that led to the emplacement of the La Soufrière de Guadeloupe dome. The debris avalanche had a volume of approximately 80 $\pm$ 40 m^3 (Komorowski, 2005; Komorowski, 2005; Lesparre et al., 2012). Since the 1530 eruption, there have been six phreatic events (Boichu et al., 2008; Feuillard et al., 1983; Peruzzetto et al., 2019; Villemant et al., 2005). The activity in 1976–77 was interpreted as a failed magmatic eruption, where a magmatic intrusion stopped a few kilometres beneath the surface, which pressurised the hydrothermal system and triggered multiple phreatic explosions (Villemant et al., 2005). The majority of the materials ejected in the phreatic explosion in 1976–77 were hydrothermally altered (Feuillard et al., 1983).

Deformation at La Soufrière de Guadeloupe, with respect to the Guadeloupe Archipelago, is continuously observed and measured by multiple permanent stations using the Global Navigation Satellite System (GNSS) (Fig. 1) from the Volcanological and Seismological Observation of Guadeloupe (OVSG-IPGP). The first measurements were taken in 1995 (Moretti et al., 2020), and, since then, multiple permanent stations have been set up around the volcano.

It is important to note the distinction between the available surface deformation data and the numerical model outputs. The GNSS data (Fig. 1) represents deformation rates (velocities in mm/yr) resulting from a complex, evolving volcanic system over decades. In contrast, the PFC model outputs represent instantaneous, time-independent displacements resulting from the mechanical re-equilibration of the rock mass under gravity. Consequently, a direct quantitative comparison between the two datasets is not possible. Instead, we use the GNSS data for a qualitative assessment of the spatial patterns of deformation (i.e., the orientation of displacement vectors) to determine where alteration-induced gravitational instability may contribute to the observed surface signal versus where other processes may be dominant.

Movement is <2 mm/yr (in the horizontal component) around the periphery of the volcano. On the summit of the lava dome, we see horizontal displacement rates of 3 to 7 mm/yr (magnitude). The largest velocity vectors reach 9 mm/year and occur on the southern flank of the dome (Moretti et al., 2020). Since the beginning of the latest unrest period at La Soufrière de Guadeloupe in 2018, concerns have increased regarding the stability of this southern flank (Moretti et al., 2020) due to the ground surface displacements. An area of particular interest on the southern flank is known as the Bulge (Fig. 1). The Bulge is a convex outward structure ‘bulging’ out of the dome and has been described and identified in multiple studies (Lesparre et al., 2012; Moretti et al., 2020; Nicollin et al., 2006; Rosas-Carbajal et al., 2017, 2016). The internal structure of the Bulge has been the subject of varying geophysical interpretations, highlighting the complexity of the region. For instance, while Lesparre et al. (2012) identified low-density anomalies using 2D muon radiography, Rosas-Carbajal et al. (2017) resolved high-density resistive rock. These apparent discrepancies likely stem from the differences in resolution and coverage between 2D radiography – which

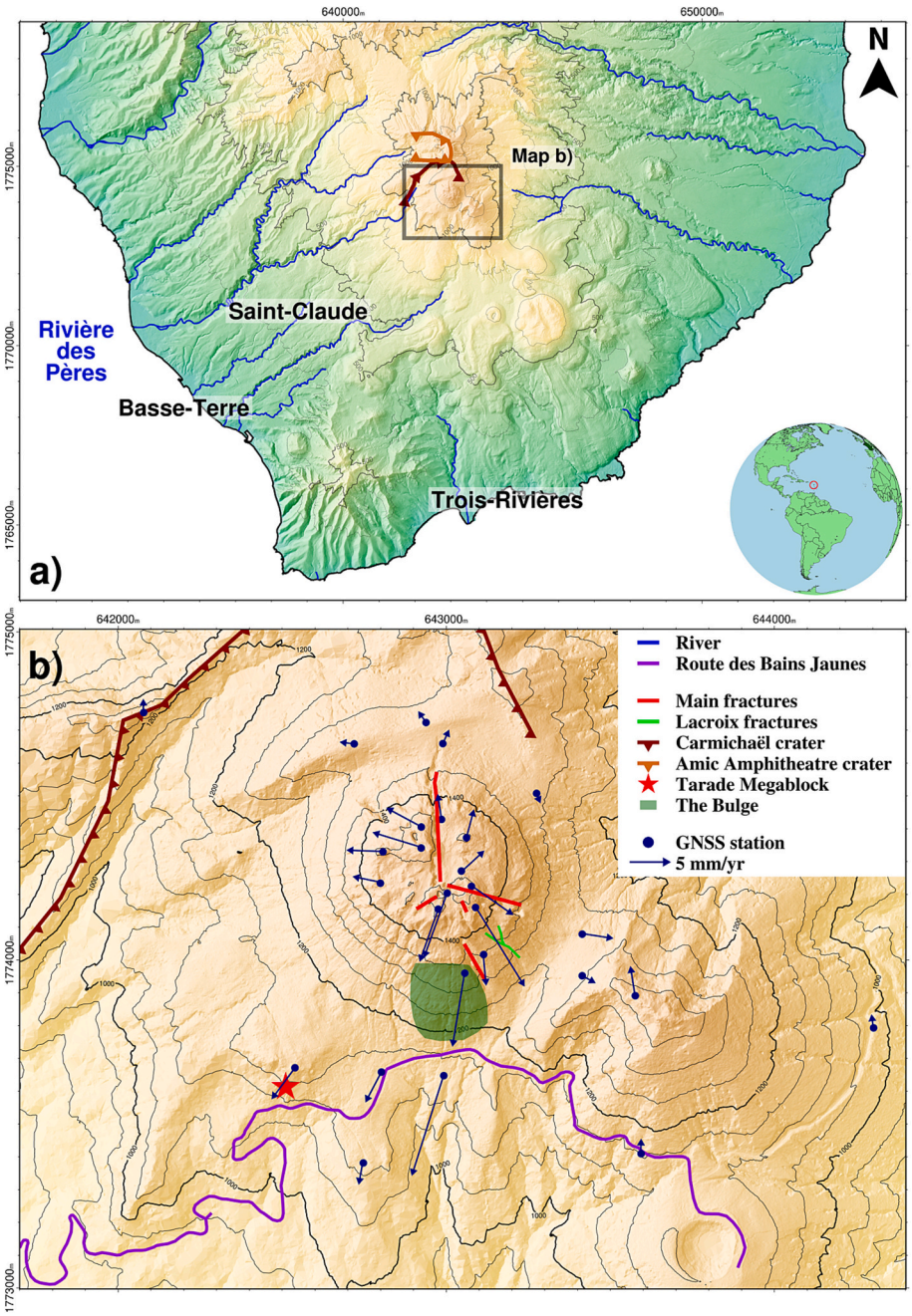

Fig. 1. Geological Setting of the La Soufrière de Guadeloupe lava dome. a) Map of the southern part of Basse-Terre. b) Map of the Grande Découverte Complex. Horizontal velocities measured by GNSS stations from 1995 to 2018, with respect to the Guadeloupe archipelago. (Map adapted from Moretti et al., 2020). The grids are given in WGS 84/ UTM Zone 20 N meters. Coastline from Global Self-consistent Hierarchical High-resolution Geography (GSHHG) (Wessel and Smith, 1996). River and road locations have been extracted from Open Street Map data (©Open-StreetMap Contributors). Digital Elevatation Model from RGE ALTI®.

integrates density along a line of sight without depth constraints – and 3D inversion methods. This observational ambiguity implies that the Bulge is likely heterogeneous, making it a critical target for stability investigation. At the surface, this region contains resistive, high-density anomalies, interpreted as unaltered rock. However, at depth (up to 100 m), parts of the Bulge consist of a low-density anomaly that lies above a highly altered zone and thus represents a potential detachment plane (Rosas-Carbajal et al., 2017, 2016). Crucially, the muon tomography data highlights that this resistive body is not homogeneous. We observe a prominent vertical zone of low density, particularly concentrated on the eastern side of the Bulge structure (Fig. 2b-c). The density deficit extends from the surface down to the limit of the reliable data (~150 m depth). Indeed, following the top of the Bulge from the north of the dome downslope, we see low density that slightly increases at ~20 m depth, and decreases again starting at ~80–100 m depth. However, a necessary caveat is that the low-density values in the deeper parts of the Bulge are likely not as well resolved as in the region below the summit, as only two muon detectors scan this zone, one of which is positioned directly in front of the anomaly. Nevertheless, the local density minimum contrasts with the higher-density regions of the surrounding dome, defining a structural heterogeneity that corresponds to an area of potential surface instability. The Bulge has been estimated to be approximately 100 m in depth from the surface (Rosas-Carbajal et al., 2016). One possible explanation for the formation of the Bulge and increasing hydrothermal fluids in the area is the compressional spreading of the southern part of the dome against the Tarade megablock on the west side

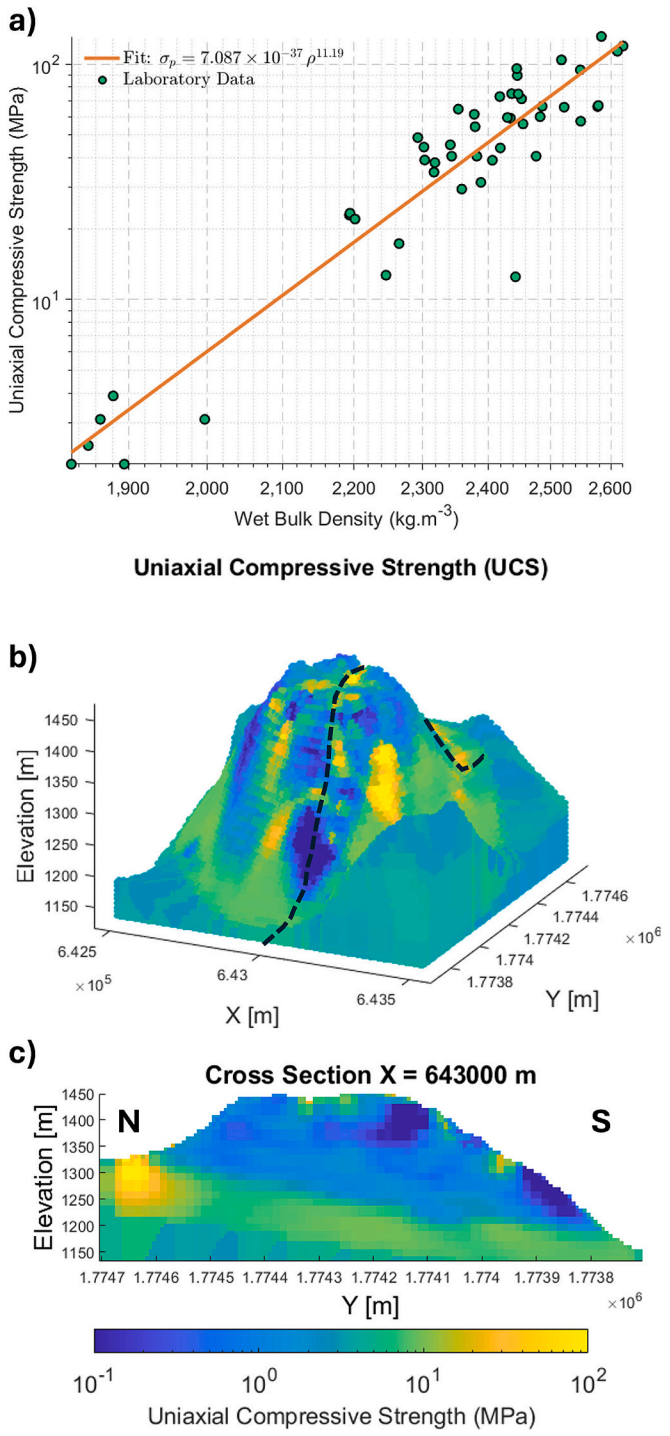

Fig. 2. Strength distribution (uniaxial compressive strength, UCS) within the La Soufrière de Guadeloupe dome where (a) shows a log-log plot of UCS as a function of bulk density (data from Heap et al., 2021b), (b) shows an overall view of the dome in 3D and (c) shows a cross section through the x-axis. The dashed line in panel (b) indicates the cross-section displayed in panel (c).

of the dome.

More recently, there have been several smaller flank collapses (occurring outside of eruptive periods) leaving collapse scars. For example, heavy rainfall in 2009 triggered a landslide that contained highly altered clay-rich material, interpreted as evidence for alteration-induced collapse (Rosas-Carbajal et al., 2016). Shallow deformation and displacements within 1000 m of the dome have been observed and linked to the shallow hydrothermal system (Moretti et al., 2020). In the last 30 years, there has been an increase in activity at fumaroles and hot springs at La Soufrière de Guadeloupe (Jessop et al., 2021; Moretti et al., 2020). Renewed fumarolic activity has been associated with increased circulation of hydrothermal fluids beneath the dome surface, thus causing pressure build-up and leading to observed ground deformation. Peruzzetto et al. (2019) suggested a partial dome collapse could impact the town of Saint-Claude, and larger collapses could affect much of the island.

3. Methods

3.1. Geophysical data

3.1.1. Data constraints

In this study, we use published data from geophysical campaigns conducted on the La Soufrière de Guadeloupe dome in 2003–2011 (Rosas-Carbajal et al., 2016) and in 2015 (Rosas-Carbajal et al., 2017). Rosas-Carbajal et al. (2016) conducted an electrical tomography survey, which identified conductive areas within the dome. Liquid-saturated rocks, particularly those with an interconnected pore network, exhibit conductivity values that are often several orders of magnitude higher than the surrounding rock matrix (Archie, 1942). Additionally, hydrothermal alteration of rocks typically leads to the precipitation of clay minerals, which are also characterised by high conductivity when wet (Qi and Wu, 2022; Waxman and Smits, 1968). Thus, when combined with geological context, electrical conductivity surveys provide valuable insights into potential locations of hydrothermal systems and hydrothermally altered rocks.

The 3D density variation within the La Soufrière de Guadeloupe dome was also mapped as gridded data (approximately 7 m resolution) using muon tomography (Lesparre et al., 2012; Rosas-Carbajal et al., 2017). Low-density anomalies were discovered within the La Soufrière de Guadeloupe dome, particularly in a zone on the southern flank where there are active fumaroles (Rosas-Carbajal et al., 2017). Typically, low-density measurements like these correspond to rock that is very porous and, therefore, mechanically weak. In combination with the conductive regions previously identified via electrical tomography (Lesparre et al., 2012; Rosas-Carbajal et al., 2016), Rosas-Carbajal et al. (2017) attributed these low-density anomalies to hydrothermally altered zones. Moreover, these potentially weaker rocks indicate that there is a higher risk for collapse on the southern flank of the dome (Rosas-Carbajal et al., 2016).

3.1.2. Uncertainty and interpretation

We acknowledge that geophysical inversions are non-unique and that the density and conductivity anomalies presented here represent one possible interpretation of the subsurface structure. For instance, low-density anomalies could plausibly represent areas of high primary vesicularity (e.g., pumiceous textures) or unconsolidated pyroclastic deposits, rather than secondary hydrothermal alteration. Similarly, high-conductivity anomalies could reflect variations in pore fluid salinity or temperature rather than the presence of alteration clays. However, we interpret these features as alteration zones due to their spatial correlation with active surface fumaroles (Moretti et al., 2020) and historical collapse scars. Critically, regardless of whether the low density arises from primary vesicularity or secondary alteration, both scenarios result in a rock mass with reduced mechanical strength. Therefore, using the density data to derive mechanical properties remains a valid approach for stability modelling, as it captures the in situ weakness of the material irrespective of its geological origin.

3.2. Discrete element method (DEM)

The models presented in this study are implemented using Particle Flow Code (PFC) software developed by the Itasca® Consulting Group. PFC employs the discrete element method (DEM) (Cundall and Strack,

1979). The DEM simulates an assembly of individual particles upon which Newton's laws of motion are calculated. These particles behave as rigid bodies and interact via contacts, with associated forces and moments updated per particle per model time step. Cohesion between particles is provided by bonds, and bond breakage represents the development of cracks within the assemblage, enabling the natural emergence of fracture systems and instabilities.

In PFC, particle interactions are governed by a variety of contact models that capture different material behaviours. In this study, we use the 'Soft-Bond Model', which allows for both force and moment to develop between bonded components. Thus, the strength of these bonds is governed by the maximum normal and shear stresses at the bond interface. If the normal stress exceeds the tensile strength of the bond, the bond fails in tension; similarly, if the shear stress exceeds the shear strength of the bond, the bond breaks, resulting in the particles becoming unbonded. Advantages to using the DEM in stability modelling include the ability to visualise large-strain problems and fracture formation, and to simulate the end members of collapse from rockfalls to dynamic failure of the full dome structure. Unlike continuum methods (e.g., the FEM), where elements typically remain connected during deformation, the DEM explicitly simulates the discontinuous nature of the rock mass. It allows for particle separation, rotation, and slip at contacts, thereby capturing how material heterogeneity – estimated here via laboratory correlations – influences the fragmentation and runout process. In addition, using the DEM, rock properties sourced from laboratory data can be incorporated into each individual inter-particle contact, such that there are millions of particles with their own unique strength (Harnett et al., 2022; Harnett and Heap, 2021). This is key, as slope stability assessments require accurate estimations of the mechanical properties, hydrology, and slope structure (Ball et al., 2018).

3.3. Correlating geophysical and mechanical data

To populate the 3D model, we estimated the 3D variation in mechanical properties from the 3D geophysical data, similar to methods in Heap et al. (2021b). To do this, we used the results from laboratory rock deformation experiments shown in Heap et al. (2023a). 293 laboratory samples were collected from around the La Soufrière de Guadeloupe dome. Notably, 8 out of the 17 blocks sampled for this study were sourced from the 2009 landslide collapse scar that was triggered by excessive rainfall (Moretti et al., 2020; Peruzzetto et al., 2019).

Mechanical properties for the model were derived from laboratory experiments performed under liquid-saturated conditions (referred to as the 'wet' dataset in Heap et al., 2021b). In this context, 'wet' refers to samples that were vacuum-saturated with distilled water prior to testing to ensure full saturation of the pore space. We deliberately selected this saturated dataset, rather than dry (samples that are oven-dried to remove all the water from within their pore space) equivalents, to reflect the realistic in-situ environmental conditions of La Soufrière de Guadeloupe. The volcano is located in a humid tropical climate characterised by high annual rainfall (Heap et al., 2023a; Komorowski, 2005), and geophysical surveys suggest the permeable dome structure is predominantly liquid-saturated (Rosas-Carbajal et al., 2016). Consequently, using dry parameters would overestimate the rock mass strength, as laboratory studies have shown that 'wet' samples are weaker than 'dry' samples (Heap et al., 2023a). The laboratory tests provided values for the key properties used in our model: bulk density, UCS, and Young's modulus. To correlate the geophysical data (muon density measurements) from Rosas-Carbajal et al. (2017) with the mechanical properties, we first established empirical power-law relationships between the saturated (wet) laboratory properties in Heap et al. (2023a): (1) bulk density and uniaxial compressive strength, and (2) bulk density and Young's modulus. We opted for power-law relationships because they reflected the general trend in the data more accurately than a linear fit. Using the saturated data, the connection between wet bulk density and both UCS and Young's modulus showed a clear nonlinear pattern, and the power-law form captured that well without overfitting. This type of relationship has also been used in similar contexts (Heap et al., 2021b), so it provided a consistent framework for comparison.

The relationships are given by the following equations:

$$\sigma_P = 7.087 \times 10^{-37} \rho^{11.19} \quad (1)$$

$$E_{mod} = 3.392 \times 10^{-35} \rho^{10.57} \quad (2)$$

where σ_P is the uniaxial compressive strength (in MPa), ρ is the wet bulk density, and E_{mod} is the Young's modulus (in GPa). We applied these relationships to the density values obtained from muon tomography, and thus have a wet bulk density, UCS, and Young's modulus values for each gridded point (approximately every 7 m) across the La Soufrière de Guadeloupe dome (see Fig. 2). We assume that the density measured by muon tomography represents a wet bulk density due to the dome being water-saturated. Previous 2D DEM models of lava domes demonstrated that water saturation reduces strength in saturated domes as alteration progresses (Heap et al., 2023a). Additionally, Heap et al. (2023a) showed that more displacement was observed in models of altered saturated domes compared to altered dry domes.

To integrate our gridded geophysical model (wet bulk density, UCS, and Young's modulus) of the La Soufrière de Guadeloupe dome with PFC, we first generate a digital terrain model (DTM) at 30 m resolution, using Shuttle Radar Topography Mission (SRTM) data (Farr et al., 2007).

The particles in PFC have an average radius of 6.5–7.5 m (to match the gridded data for better interpolation) but follow a uniform size distribution from a minimum of less than 1 mm to a maximum radius of approximately 15 m (see Supplementary Fig. S1 for the radius distribution). Therefore, the maximum radius matches the resolution of the DTM. We populate this DTM in PFC with discrete elements (particles). While the active dome material is governed by the 'Soft-Bond Model', the 'Linear Model' is applied at the boundary between the topography and the domain extent. This friction-only model simulates an extended topography beyond the limits of the model domain. Particle contacts at the domain boundary are fixed to maintain consistency with the digital terrain model (DTM) of the volcanic dome and its surrounding terrain. Model probing and testing occur well inside the domain, far from the fixed boundary, to ensure that observed deformations are driven by the experimental conditions rather than boundary effects.

Next, we perform a nearest neighbour interpolation between the geophysical data points and the elements in PFC to obtain continuous data for the mechanical heterogeneity within the dome. We performed an interpolation due to the geophysical data being gridded, whilst the discrete elements in PFC are of various sizes and are packed by Voronoi tessellation. Nearest neighbour interpolation helped avoid unnatural artefacts and smooth transitions that were inconsistent with the natural data variation.

Our model domain is larger than the extent of the geophysical data; therefore, some material falls outside the region of known mechanical properties. Thus, any points that fall outside the bounds for interpolation are given an average modal value based on the geophysical data. This ensures that the boundary between the heterogeneous dome and the rest of the topography does not represent a large discontinuity. The gridded data are capped at a UCS of 131.3 MPa (Fig. 2a) to ensure that the model does not consider unrealistically high numbers from the empirical power-law relations (for the range of dome values, see Table S2 in the Supplementary Material). Thus, the maximum density (2629 kg/m^3) and Young's modulus (55 GPa) in the model correspond with the capped UCS, based on their power-law relations (see Supplementary Fig. S2).

For the purpose of this study, we assume that the UCS is equivalent to inter-particle bond cohesion. Due to the model consisting of millions of contacts, it was not realistic to calibrate UCS tests for each particle. We acknowledge that this simplification assigns an artificially high cohesive strength to the bonds, as macroscopic UCS typically exceeds true cohesion due to the contribution of internal friction. The 'strong'

material parameterisation is complemented by our treatment of the rock mass structure. Although surface structural features are mapped (Fig. 1), they were not explicitly included in the 3D model geometry because the 3D attributes of these features – specifically their dip, depth extent, thickness, and displacement – are unconstrained at depth. To avoid introducing unquantified geometric errors by assuming these parameters, we adopted a continuum approach where rock mass degradation is inferred from density distributions rather than discrete defect modelling.

Combining both approaches manages the trade-off between aleatoric (natural variability) and epistemic (lack of knowledge) uncertainty. By prioritising the aleatoric uncertainty captured by the laboratory-derived density-strength correlations over the epistemic uncertainty of unconstrained fault geometries, and assigning an upper-bound cohesive strength, we ensure that our model represents a conservative, 'strong' end-member scenario. Therefore, the significant displacements and instabilities we observe occur despite this overestimated strength, reinforcing the potential severity of the alteration-induced hazard. Once the interpolation between the gridded data and PFC contacts is completed, we input the values obtained for each property into PFC. It is important to note that the bulk density is attributed to the particles in PFC, whereas cohesion and Young's modulus are applied to the inter-particle contacts. In addition, we set the tensile strength of each contact to one-tenth of the cohesion value, reflecting the typical ratio between compressive and tensile strength in geological materials (Cai, 2010; Heap et al., 2022). To simulate the frictional resistance between particles within the rock mass, we assigned a constant inter-particle friction coefficient of 0.58 (equivalent to a friction angle of 30°) to all contacts. Our model, as shown in Figs. 2b-c, includes over 800,000 elements connected by 5 million contacts. The initial model state therefore incorporates full heterogeneity as informed by the geophysical data. 56% of the modelled dome has a strength less than 5 MPa, and 93% falls below 10 MPa.

We also construct a homogeneous dome model in which the values of bulk density, UCS, and Young's modulus are constant across the entire dome, providing a baseline for comparison with the heterogeneous model. During model generation, we assign a wet bulk density, cohesion, tensile strength, and Young's modulus to the balls and contacts, respectively. These values are derived as a representative modal value for each parameter, ensuring they reflect the typical properties of the dome (see Table S2 in the Supplementary material).

3.4. Settling the model topography

To ensure the model reaches a quasi-static equilibrium before alteration is introduced, we initially settle the model until the ratio of the maximum unbalanced forces to the average force on each element is below 1×10^{-5}. This is a dimensionless threshold commonly used in DEM modelling to ensure the system has reached a stable state. We chose this tolerance as the particle displacements produced were in alignment with the desired order of displacement magnitude of approximately 1 mm. After the heterogeneous contact properties are assigned, we gravitationally settle the model until each particle shows displacement vectors to be <1 mm. This threshold is lower than the smallest velocity vectors from the GNSS data at approximately 2 mm/yr, guaranteeing that any movement that is on the mm scale or above is a result of variable manipulation during testing.

3.5. Implementing alteration within the models

To model weakened alteration zones, we reduce the cohesion and tensile strength on each contact to a certain percentage (50% or 10%) of their original values. We correlate the reduced cohesion value with the corresponding Young's modulus using a power-law relation (see Supplementary Fig. S2c). The power-law relation is obtained by correlating the UCS and Young's Modulus values calculated in Eqs. (1) and (2) from the muon density data (see Supplementary Fig. S2a-b). These reduced correlated parameters are then assigned to the contacts in PFC to reduce the overall rock strength (see Supplementary Table S2 for average values). We therefore apply the reduction in strength as a modification of the material state within a quasi-static, time-independent framework. While natural hydrothermal alteration in nature is not instantaneous, our model lacks the temporal calibration required to quantify a specific rate of degradation. Consequently, rather than simulating the process of alteration, our simulation represents the final mechanical state of the rock mass following weakening. This approach allows us to assess the stability of the defined alteration scenarios without introducing arbitrary, unconstrained time scales. Robust alteration rate data, when available, would provide the means to do this. After the weakening is applied, the model is run for 10,000 cycles to ensure dissipation of any dynamic effects. Models of a reduction to 10% strength of the original strength could be interpreted to show progression in alteration (i.e., after a longer time period) than the reduction to 50% strength. However, it is important to note that factors other than time, such as fluid composition and pH, can also influence the extent of alteration.

Our models focus on two key weakening zones: (1) the Bulge; and (2) the entire southern flank of the dome. Firstly, we selected the Bulge for localised weakening. The lateral dimensions of this zone (245 m × 275 m) were defined based on the surface boundaries of the Bulge deformation sector as mapped by Moretti et al. (2020) (shown in Fig. 1) and Rosas-Carbajal et al. (2016). For simplicity of modelling, we idealised this surface feature into a rectangular volume. While this geometry is a simplification, it fully encapsulates the prominent low-density vertical column observed in the eastern sector of the Bulge (Fig. 2). However, we note that the extremity of the low-density values at depth is likely owed to an artefact, as this region is scanned by fewer detectors, with one station located directly in front of the structure. We constrained the depth of this zone to the upper 150 m, consistent with the resolution limits of the muon telescope data in this sector (Rosas-Carbajal et al., 2017). Secondly, we modelled the southern flank (855 m × 535 m) to test a 'worst-case scenario'. This larger domain was selected because the southern flank is identified as the most altered and unstable sector of the dome. Moretti et al. (2020) highlight this area as the locus of maximum surface deformation. Structurally, Rosas-Carbajal et al. (2016) demonstrated via electrical resistivity tomography that the main hydrothermal reservoir is concentrated beneath this flank. Furthermore, recent 3D strength modelling by Heap et al. (2021b) confirms that this region represents the largest continuous volume of low-strength material within the edifice. Finally, hazard assessments by Peruzzetto et al. (2019) have specifically isolated this flank as the primary candidate for a partial edifice collapse.

3.6. Strain

We perform inverse strain modelling (i.e., fitting strain to displacement data) in our models to help visualise localisation of displacement; the strain particularly highlights where particles move relative to their neighbours, thus allowing visualisation of potential detachment planes or faults.

We adapt the 2D method from Schöpfer et al. (2007) for use in 3D. This method calculates the Cauchy-Green deformation tensor, and thus, the Lagrangian strain tensor, considering the finite shear strain theory (Cardozo and Allmendinger, 2009; Schöpfer et al., 2006). For each particle i, with x_i, y_i, z_i the particle location, and u_i, v_i, w_i the particle displacement, there are N neighbouring particles, with x_j, y_j, z_j representing the neighbouring particle location, and u_j, v_j, w_j representing the neighbouring particle displacement. Then, we consider an area that surrounds the particle and its neighbouring particles. The positions of these neighbouring particles are calculated relative to the original particle to classify homogeneous strain. The displacement fields of the neighbouring particles are written as:

$$\overline{u}_j = a_i(x_j - x_i) + b_i(y_j - y_i) + c_i(z_j - z_i)$$

$$\overline{\boldsymbol{v}}_j = d_i(x_j - x_i) + e_i(y_j - y_i) + f_i(z_j - z_i)$$

$$\overline{\boldsymbol{w}}_j = g_i(x_j - x_i) + h_i(y_j - y_i) + i_i(z_j - z_i) \quad (3)$$

$\overline{\boldsymbol{u}}_j$, $\overline{\boldsymbol{v}}_j$, $\overline{\boldsymbol{w}}_j$ are the homogeneous displacement approximations for which x_j, y_j, z_j are their evaluations. Thus, the goal is to calculate the best-fit coefficients, as these are, by definition, the components of the displacement gradient tensor (Green tensor):

$$\boldsymbol{G_i} = \begin{bmatrix} a_i & b_i & c_i \\ d_i & e_i & f_i \\ g_i & h_i & i_i \end{bmatrix} \quad (4)$$

To calculate the best-fit coefficients, we apply the least-squares procedure to each row of the Green tensor. From there we get the strain tensor:

$$\boldsymbol{A_i} = \frac{1}{2}(\boldsymbol{G_i} + \boldsymbol{G_i}^\top) \quad (5)$$

and the Lagrangian strain tensor (i.e., deviations from identity matrix δ):

$$\boldsymbol{E_i} = \frac{1}{2}(\boldsymbol{G_i}^\top \boldsymbol{G_i} + \delta) \quad (6)$$

Finally, the maximum shear strain can be extracted from $\boldsymbol{E_i}$ for each particle, e.g.,

$$\gamma_{max} = \frac{1}{2}(E_{max} - E_{min}) \quad (7)$$

where E_{max} and E_{min} are the maximum and minimum principal strains computed as the eigenvalues of the Lagrangian strain tensor.

3.7. Collapse volumes and runout modelling

Finally, we quantify the volume of material displaced after running each weakening model, measuring the volume of material that has been displaced more than 1 cm, 10 cm, 1 m, 2 m, 5 m, and 10 m. We use the material volume that displaced >10 cm for runout modelling using VolcFlow, which enables us to calculate runout distance and flow paths for our collapse scenarios.

VolcFlow uses a finite-difference Eulerian code written in MATLAB and takes a depth-averaged approach (equations of mass and momentum) to model isothermal geophysical flows (Kelfoun et al., 2009; Kelfoun and Vallejo Vargas, 2016). VolcFlow has been applied in a variety of volcanic contexts, including modelling landslides (Kelfoun et al., 2009), lava flows (Kelfoun and Vallejo Vargas, 2016), pyroclastic density currents (Kelfoun et al., 2009), and rock avalanches (Kelfoun et al., 2009). VolcFlow assumes a fixed collapse volume, meaning no material is picked up or redistributed during the flow; the volume is predefined and added in its entirety.

In our VolcFlow model, we employ a plastic rheology (constant retarding stress). Here, the basal friction angle is set to zero. Consequently, the flow resistance is determined entirely by the cohesion parameter, which acts as a constant yield strength. We assume a yield strength of 5000 Pa, a standard value for volcanic debris avalanches (e.g., Kelfoun et al., 2009), and the same representative bulk density obtained for our heterogeneous models of 1891.73 kg/m^3. We use resampled TanDEM-X data to generate a higher resolution (10 m) DTM in VolcFlow, isolating the collapse volume determined by our DEM models. To set up the VolcFlow model, we first import the positions of each ball particle that is displaced by more than 10 cm into MATLAB. Using these positions, we determine the maximum and minimum elevation of the collapse volume within each grid cell (tile on a 2D surface). A modified DTM is then created by subtracting the collapse volume from the original TanDEM-X elevation data. From this, we compute a flow thickness matrix, which represents the spatial distribution of material available to flow. This matrix is then used as the initial input for the VolcFlow simulation.

The VolcFlow simulations then provide debris avalanche flowpaths, including flow thickness and runout distance. Although a 30 m DTM was sufficient for the initial PFC modelling given particles with an average radius of 6.5–7.5 m, a higher-resolution DTM was used for the runout modelling to better capture small-scale topographic features that can influence flow behaviour. It is important to note that the primary aim of this study is to develop a workflow that integrates DEM-based collapse modelling with flow runout simulations. Therefore, the parameters used in VolcFlow are kept intentionally basic and do not include flow properties specific to La Soufrière de Guadeloupe, aside from the bulk density. This approach is designed to demonstrate the workflow rather than to replicate the detailed, site-specific modelling performed by other researchers.

4. Results

Here, we present the results of models that investigate: (1) the effect of increasing alteration-induced weakening in a volcanic dome, (2) the effect of varying the spatial extent of a mechanically weakened zone and (3) the resulting collapse volumes from various alteration scenarios. The displacement and finite shear strain values are calculated for the full 3D model, but in some figures, are shown in cross-section for a more comprehensive understanding of the processes occurring in the subsurface. Each alteration scenario is associated with a model number (see Table 1) for ease of understanding. The associated collapse volume for each model is also displayed at each threshold (described further in Section 4.3).

4.1. Effect of alteration-induced weakening on deformation

We first explore the effect of weakening a 150 m thick surface zone on the southern flank of the dome, representative of the Bulge (Fig. 3). We weaken the rock in this region to both 50% (see Table 1, model 1) and 10% (see Table 1, model 2) of its original strength, which is well supported by studies conducted by Heap et al. (2021b) and Darmawan et al. (2022). For the scenario where the rock has been weakened to 50% of the original values (Fig. 2a), we observe maximum displacements of 1.02 m. Most displacement occurs to the east of the Bulge. Displacement also occurs towards the crest of the dome, outside the zone of weakening. The cross-section of this model is shown in Fig. 3b, where the largest displacements are seen at the surface. Displacements of ~1 cm can be observed up to 100 m below the surface.

Displacements of ~1 cm can be observed up to 100 m below the surface. In the model with rock properties weakened to 10% of their original values (Fig. 3c), the maximum displacement is 20.02 m. Displacement is observed on the southern flank as well as to the northwest of the Bulge and towards the crest of the dome, showing that displacement again occurs outside of these weakened zones. In cross-section (Fig. 3d), displacements of 1 cm are observed over 200 m in depth, significantly deeper than the weakened zone.

Analysis of shear strain provides insight into how slope failure and internal deformation evolve in structurally weakened dome models. Shear strain is visualised in Fig. 4 for the same models presented in Fig. 3 (models 1 and 2). For the model weakened to 50% of the original rock strength (Figs. 3a-b), high shear strain is observed at the crest of the dome, suggesting fracturing towards the apex of the dome (Fig. 4a). The diffuse high shear strains in the centre of the weakened zone suggest slope disaggregation in a wedge-like shape. The pattern beneath the initial disaggregation shows the development of multiple rotational failure planes. The shear strain here is due to the material moving southward and slipping downslope.

Fig. 4b shows the induced-weakening scenario in Figs. 3c-d, where the rock properties are reduced to 10% of their original values (model 2). In Fig. 4b, we visualise shear strain on a scale bar from 0 to 1×10^{-3} m, as there is a higher magnitude of deformation in this model. There is

Table 1
Details of each model presented in this paper. Each model corresponds with a model number and is displayed as a schematic illustrating the spatial extent of weakening and the proportional reduction in rock strength. We show the volume (m^3) displaced between each threshold for each model. The total collapse volumes indicate the sum of material displaced for each threshold.

Alteration Model		Bulge: Strength 50%, Thickness 150m	Bulge: Strength 10%, Thickness 150m	Bulge: Strength 10%, Thickness 50m	Whole Flank: Strength 50%, Thickness 150m	Whole Flank: Strength 10%, Thickness 150m	Whole Flank: Strength 10%, Thickness 50m
Model Number		1	2	3	4	5	6
Model Schematic							
Volume Displacement Across Thresholds (x 10^6 m^3)	0.01 m ≤ x < 0.1 m	0.84	19.64	6.18	13.38	103.55	24.67
	0.1 m ≤ x < 1 m	0.090	1.27	0.49	0.16	16.65	5.05
	1 m ≤ x < 2 m	0.0021	0.070	0.061	0.0021	0.20	0.11
	2 m ≤ x < 5 m	0.00	0.12	0.10	0.00	0.16	0.17
	5 m ≤ x < 10 m	0.00	0.066	0.064	0.0014	0.13	0.11
	x ≥ 10 m	0.00	0.022	0.019	0.00	0.050	0.027
	Total >0.01 m	0.93	21.18	6.91	13.55	120.74	30.14
	Total >0.1 m	0.092	1.54	0.73	0.16	17.19	5.47

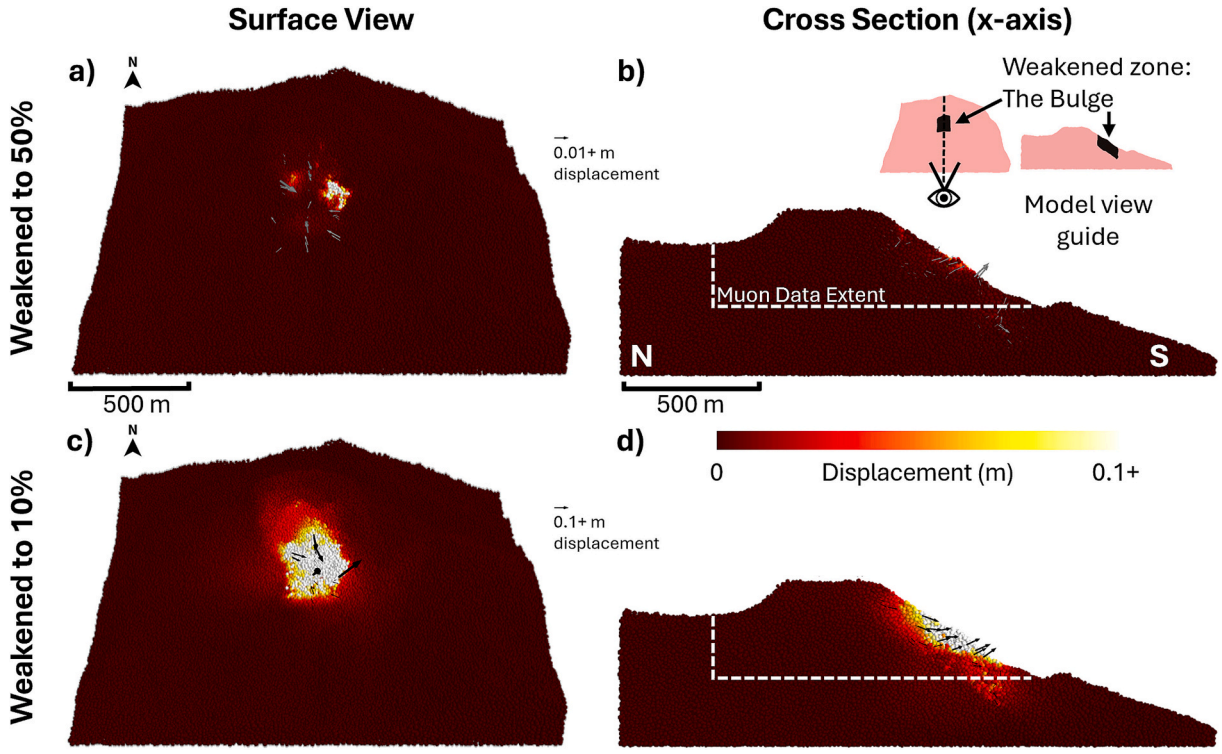

Fig. 3. Displacement models simulating a 150 m thick weakened zone in the Bulge region. (a)-(b) Show the surface view and cross section (across the x-axis) for zone weakening to 50% of the original rock strength (model 1), and (c)-(d) show a surface view and cross section for zone weakening to 10% of the original rock strength (model 2). The dashed line indicates the extent of the area in which we have the muon tomography density data. Displacement is shown from 0 to 10 cm and capped above this for the purpose of visualisation. The colour scale is chosen to highlight larger displacements. Displacement vectors are normalised and limited to a maximum magnitude of 0.1 m. For visualisation purposes, vector lengths are scaled by a factor of 500 in panels (a) and (c), and by a factor of 50 in panels (b) and (d). Thus, a plotted arrow length of 500 units in (a) and (c), or 50 units in (b) and (d), represents a real displacement of at least 0.1 m.

significant shear strain at the crest of the dome (approx. an order of magnitude higher than in Fig. 4a) that is observed outside the initial weakened zone, suggesting that the effects of weakening in the Bulge can graduate to detachment upslope. Disaggregation is pervasive throughout the weakened zone. There are more curved planes of strain accumulation below the weakened zone, and they are more strongly

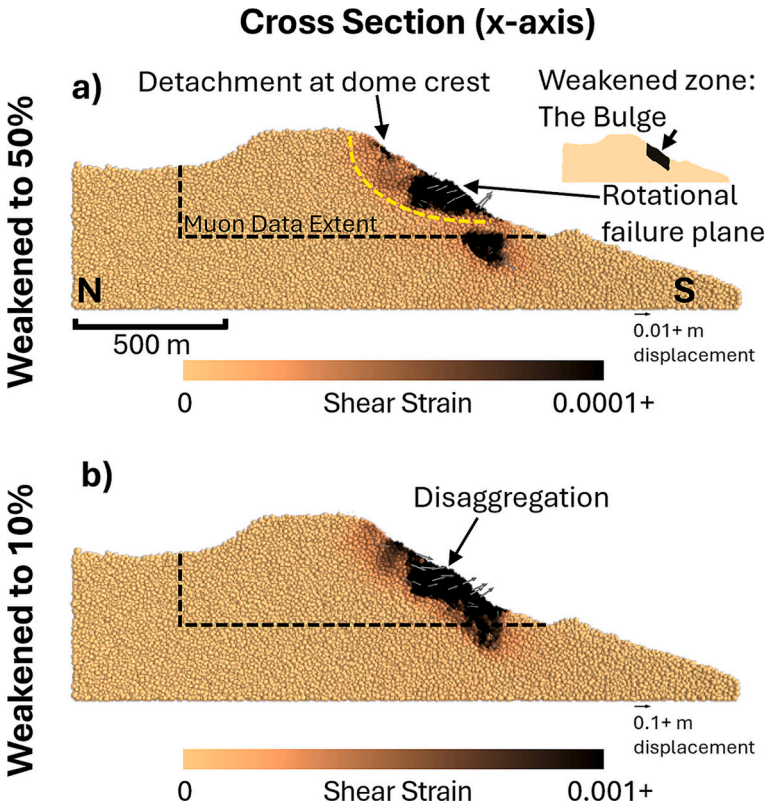

Fig. 4. 3D finite shear strain modelling in cross-section, for a 150 m thick alteration zone in the Bulge region. The bulk strength is reduced to (a) 50% (model 1) and (b) 10% of its original strength (model 2). (a) Shows finite shear strain on a lower order of magnitude than (b) to highlight deformation patterns. The dashed black line indicates the extent of the area in which we have the muon tomography density data. The yellow dashed line indicates the location of a potential rotational failure plane. Displacement vectors are normalised and capped at 0.1 m (10 cm). For visualisation purposes, vector lengths are scaled by a factor of 500 in panel (a), and by a factor of 50 in panel (b). Thus, a plotted arrow length of 500 units in (a), or 50 units in (b), represents a real displacement of at least 0.1 m.

defined than in Fig. 4a.

4.2. *Effect of varying the spatial extent of the alteration zone*

Next, we investigate how the size, location and thickness of the weakened zones impact dome stability, considering zones that cover (1) the Bulge (245 m × 275 m) and (2) the entire southern flank (855 m × 535 m). The altered zones are given thicknesses of both 50 m and 150 m. We simulate these two distinct depth scenarios to represent different rock-weakening mechanisms. The 'deep' (150 m) model encompasses the full vertical extent captured by the muon data, and critically, the observed low-density column. In contrast, the 'shallow' (50 m) model serves as an end-member and is designed to test hazard scenarios resulting from any mechanism that mechanically degrades rock within the vadose zone (above the water table). The most pervasive of these drivers is the chemical 'scrubbing' of rising magmatic gases (SO_2 and HCl). Scrubbing occurs when hot volcanic gas intersects the shallow groundwater table; the water effectively absorbs the gas, creating highly acidic condensates that aggressively degrade the host rock within the vadose zone (Villemant et al., 2014). The chemical reaction results in advanced argillic alteration, replacing competent andesite with mechanically weak minerals such as alunite and kaolinite (Salaün et al., 2011).

Distinct from this chemical weathering, physical mechanisms operate as independent drivers of instability. For instance, the dome's structural integrity is inherently compromised by dense networks of cooling joints (Nicollin et al., 2006). Furthermore, the slope is subject to intense tropical rainfall, which saturates the porous shallow layer and critically reduces effective stress, triggering failure regardless of alteration state (Moretti et al., 2020). Therefore, by assigning reduced strength parameters to the top 50 m, our 'shallow' model serves as a mechanical proxy for this cumulative degradation – whether induced by chemical, structural, or hydrological processes. This approach is validated by our simulation results, which show some of the greatest displacements concentrated specifically in this surficial layer. In addition, this mirrors the morphology of historical shallow collapse scars observed on the volcano.

For all models shown in Fig. 5, we reduced the rock properties to 10% of their original strength. For the 150 m-deep weakened Bulge (see Table 1, model 2, Fig. 3c-d, and Fig. 4a), the maximum displacement is 14.64 m, with the largest displacements observed near the surface. The maximum displacements are observed to the east of the Bulge (see surface view in Supplementary Fig. S3a). Displacement is observed above the altered zone towards the crest in Fig. 5a, and displacements of >1 cm are observed up to a depth of 120 m. In Fig. 5b, despite the weakened zone only extending to a depth of 50 m (see Table 1, model 3), displacements of 1 mm can be observed up to 300 m below the surface. In Fig. 5c-d, we weaken the entire southern flank of the dome, rather than just the Bulge. This is because the southern flank is the most unstable portion of the dome and is thought to be the most pervasively altered (Heap et al., 2021b; Rosas-Carbajal et al., 2017, 2016). The alteration zone in Fig. 5c (see Table 1, model 5) is 150 m deep and we observe maximum displacement of 24.74 m. Displacements of over 20 m are seen both to the east of the Bulge (see surface view in Supplementary Fig. S3) and at the peak of the dome (Fig. 5c). At the top of the alteration zone, displacements of >10 cm are observed up to a depth of 150 m, but at the bottom, displacements are smaller and range from 3 cm to 8 cm (Fig. 5c). Smaller displacements of 4–5 cm are observed upslope of the alteration zone at the peak of the dome (Fig. 5c).

Finally, the model in Fig. 5d (see Table 1, model 6) represents

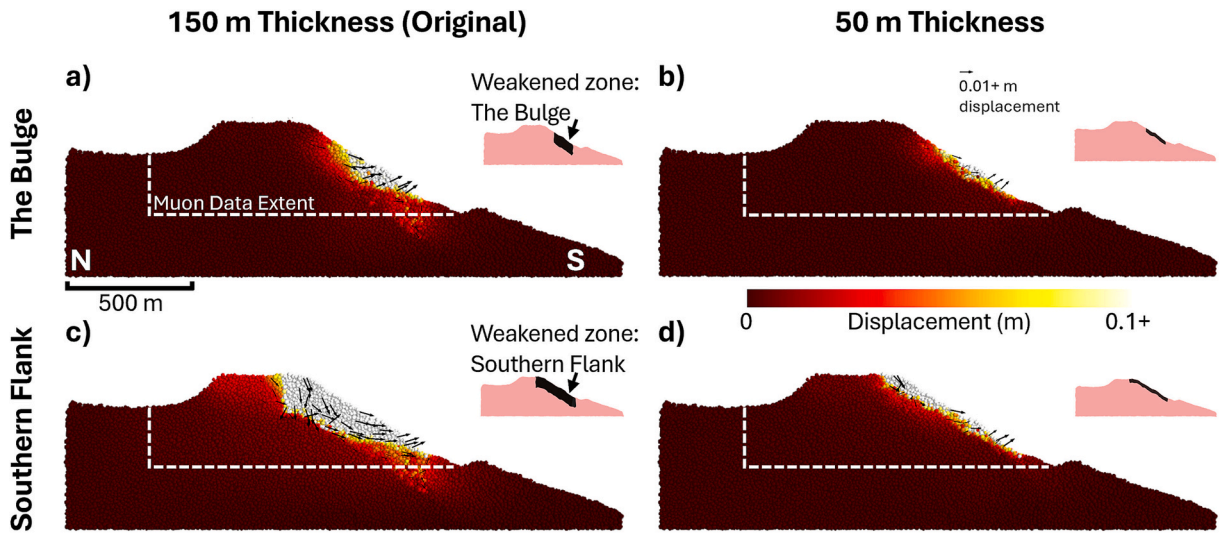

Fig. 5. Models demonstrating the effect of varying the spatial extent of a mechanically weakened zone, all reduced to 10% of their original bulk strength. We show cross sections (across the x-axis) for models weakening the Bulge to (a) 150 m depth (model 2), and (b) 50 m depth (model 3), and models weakening the Southern Flank at (c) 150 m depth (model 5), and (d) 50 m depth (model 6). We show displacements from 0 to >10 cm. The dashed line indicates the extent of the area in which we have the muon tomography density data. Displacement vectors are normalised and limited to a maximum magnitude of 0.1 m (10 cm). For visualisation purposes, vector lengths are scaled by a factor of 50. Thus, a plotted arrow length of 50 units represents a real displacement of at least 0.1 m.

alteration across the entire southern flank of the dome, with a shallower zone extending to a depth of 50 m. This model produced the highest maximum displacement of 26.31 m, despite having a shallower alteration zone than in Fig. 5c. The maximum displacement was recorded at the top of the dome. The area to the east of the Bulge again also shows displacements over 10 m. Displacements of ~8 mm (see Supplementary Fig. S4d) are observed on the northern flank of the dome, near the summit. Displacements greater than 1 mm can be observed up to 450 m depth. This is a greater depth than in the model shown in Fig. 5b, when we look at shallow (50 m) mechanical weakening solely in the Bulge. The same displacement field is shown in Supplementary Fig. S4, but with the colour scale adjusted to visualise lower-magnitude deformation. While Fig. 5 clips the data at 10 cm to emphasise significant displacements, Supplementary Fig. S4 clips the data at 1 cm to reveal finer-scale patterns that are otherwise obscured.

Fig. 6 shows the shear strain for the models presented in Fig. 5. Shear strain is visualised on the same scale for each of the four models but is shown at a lower order of magnitude in supplementary Fig. S5 for a more detailed view of specific features. In Fig. 6a-b, we visualise strain for models in which only the Bulge was weakened (models 2 and 3). In Fig. 6a, we can see the curved planes that suggest rotational slumping towards the base of the weakened zone. However, the majority of high shear strain values are visible as disaggregation towards the surface in a part of the topography that protrudes outward. The areas of highest shear strain in all model visualisations typically correspond to the weakest parts in the topography with the lowest rock strength and Young's modulus. In Fig. 6b, the maximum shear strain is seen near the surface, similar to Fig. 6a. Lower shear strain values cluster in a circular shape beneath the Bulge altered zone. Detachment planes stretch from the peak of the dome towards the bottom of the slope in the south.

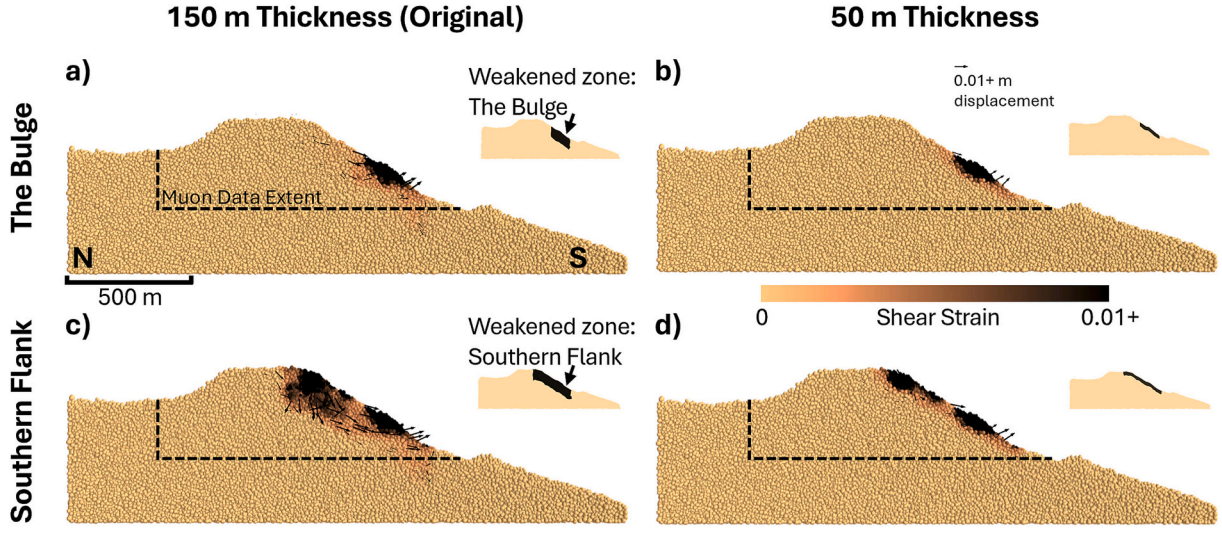

Fig. 6. 3D finite shear strain models demonstrating the effect of varying the spatial extent of a mechanically weakened zone, all reduced to 10% of their original bulk strength. We show cross sections (across the x-axis) for models weakening the Bulge to (a) 150 m depth (model 2), and (b) 50 m depth (model 3), and weakening the Southern Flank at (c) 150 m depth (model 5), and (d) 50 m depth (model 6). We show finite shear strain values from 0 to >0.01. The dashed line indicates the extent of the area in which we have the muon tomography density data. Displacement vectors are normalised and limited to a maximum magnitude of 0.1 m (10 cm). For visualisation purposes, vector lengths are scaled by a factor of 50. Thus, a plotted arrow length of 50 units represents a real displacement of at least 0.1 m.

In Fig. 6c-d, we visualise shear strain for models with weakening of the entire southern flank (models 5 and 6). In Fig. 6c, the magnitude of shear strain is a lot higher than in the other models (in Fig. 6 a, b and d). High shear strain is observed deeper within the dome, due to the deeper alteration zone. The strain distribution appears more "patchy" than in other models. The top of the weakened zone suffers more shear strain than the bottom. This again suggests that the risk of instability increases upslope. The lowest shear strain values within the weakened zone occur directly below the high shear strain disaggregation in the region where the topography protrudes outwards (Fig. 6c). Finally, in Fig. 6d, we see that the crest of the dome exhibits the highest shear strain values. In all models, at smaller scales, detachment planes are visible along horizontal, angled, parallel lines (see Supplementary Fig. S5d). These detachments extend from the rear of the weakened zone to the back of the dome. The failure progresses incrementally, with the material slipping in discrete sections. This detachment pattern suggests shear fracture propagation, with the material separating progressively along planes of weakness, indicating a gradual delamination process rather than a sudden, complete failure.

4.3. Collapse volumes

In Fig. 7, we present the scenarios for which we observe the minimum and maximum volumes displaced over 1 cm. In Fig. 7a, the model with the least overall displacement (smallest collapse volume) corresponds to the scenario where material in the Bulge is weakened to 50% of its original strength (see Table 1, model 1), and the weakened zone extends to a depth of 150 m (Figs. 3a-b, 4a). The total volume displaced >1 cm is 0.93×10^6 m^3 and by >10 cm is 0.092×10^6 m^3. In contrast, Fig. 7b shows the model with the largest volume displaced, which is observed where the entire southern flank is reduced to 10% strength (see Table 1, model 5, Fig. 4c, and 5c). The total volume displaced by >1 cm is 120.74×10^6 m^3, 130 times the model with the least displacement, and a total of 17.19×10^6 m^3 displaces >10 cm, 187 times the model with the least displacement.

For each model, we quantify the volume of material that has displaced over 1 cm, 10 cm, 1 m, 2 m, 5 m, and 10 m. Fig. 8a presents a stacked bar chart that quantifies the total collapse volume that displaced between each threshold. For example, model 5 (see Table 1) corresponds to the model with both the maximum displacement of all models, and the largest collapse volume (shown in Fig. 7b). Model 1 (see Table 1) corresponds to the model with the smallest collapse volume (shown in Fig. 7a). Fig. 8b illustrates the proportion of the total cumulative displaced volume that surpassed each threshold in each model. In most cases, approximately 90% of the material displaced between 1 cm and 10 cm. However, in model 5 (see Table 1, Fig. 8a), 103.55×10^6 m^3 of material was displaced between 1 cm and 10 cm. In model 1, a much smaller volume of 0.84×10^6 m^3 displaced between 1 cm and 10 cm; however, both values represent a similar proportion of the total displacement volume within that model. We established a threshold of 10 cm to define the unstable collapse volume. Given that the PFC model simulates a time-independent, quasi-static response, this magnitude serves as a conservative filter to distinguish the actively mobilised mass from minor elastic deformation and background settling. While surface creep can accumulate to this magnitude over decades, in our quasi-static simulations, this displacement represents a coherent volume of instability. Furthermore, this threshold yields collapse volumes (0.09–17.19×10^6 m^3) that align with the range of scenarios considered in previous hazard assessments (e.g., Peruzzetto et al., 2019), validating it as a realistic proxy for the onset of failure. Therefore, the input for our VolcFlow runout modelling consists of the total volume (the sum of each threshold combined) that displaced ≥10 cm. Thus, our maximum collapse volume is 17.19×10^6 m^3, and our minimum is 0.092×10^6 m^3. For a table of all displacement volumes, see Table 1.

5. Discussion

The results of this study primarily highlight the effect of hydrothermal alteration on volcanic dome stability, collapse volumes, and runout distances. Our results investigate the effect of mechanical rock weakening by varying (1) the amount of alteration-induced weakening, and (2) the spatial extent of the weakened zone.

5.1. Effects of alteration

Our results show that increasing the alteration-induced weakening results in greater displacements, agreeing with previous findings for 2D models (e.g., Heap et al., 2021b). The maximum displacement in the models reduced to 10% strength (Fig. 3c-d) was almost 20 times that of the models reduced to 50% strength (Fig. 3a-b). This is in agreement with previous studies that show that lower rock strength results in increased dome instability, and thus, higher displacements (Harnett et al., 2022; Harnett and Heap, 2021). Damage is typically more severe and more spatially widespread with increasing alteration (Heap et al.,

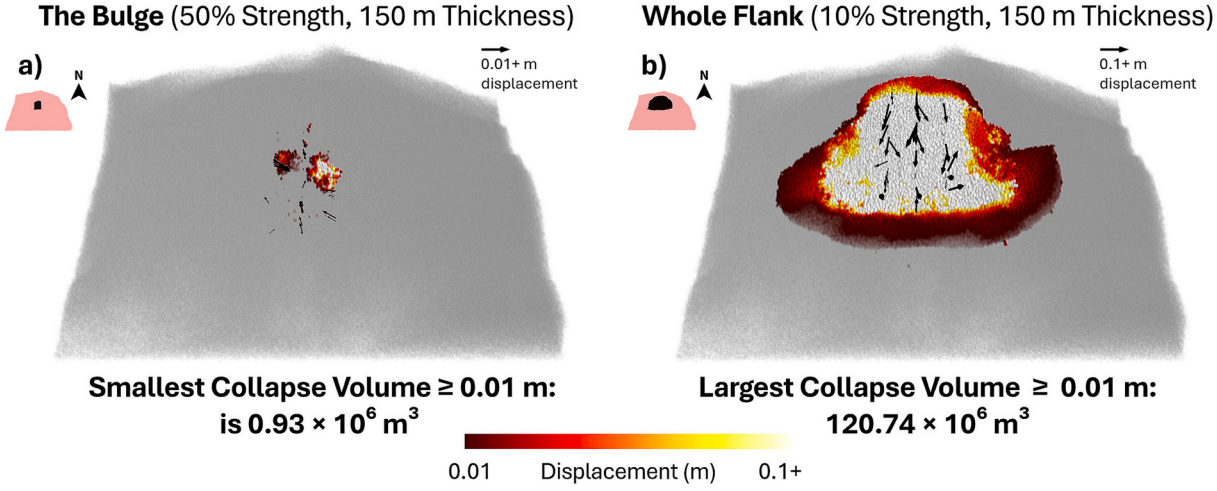

Fig. 7. Models illustrating collapse volumes resulting from mechanical rock weakening, with displacements ranging from 1 cm to 10 cm on the colour bar. (a) shows the smallest recorded collapse volume from our tested scenarios (model 1), while (b) shows the largest collapse volume from our tested scenarios (model 5). Displacement vectors are normalised and limited to a maximum magnitude of 0.1 m (10 cm). For visualisation purposes, vector lengths are scaled by a factor of 1500 in panel (a), and by a factor of 150 in panel (b). Thus, a plotted arrow length of 1500 units in (a), or 150 units in (b), represents a real displacement of at least 0.1 m.

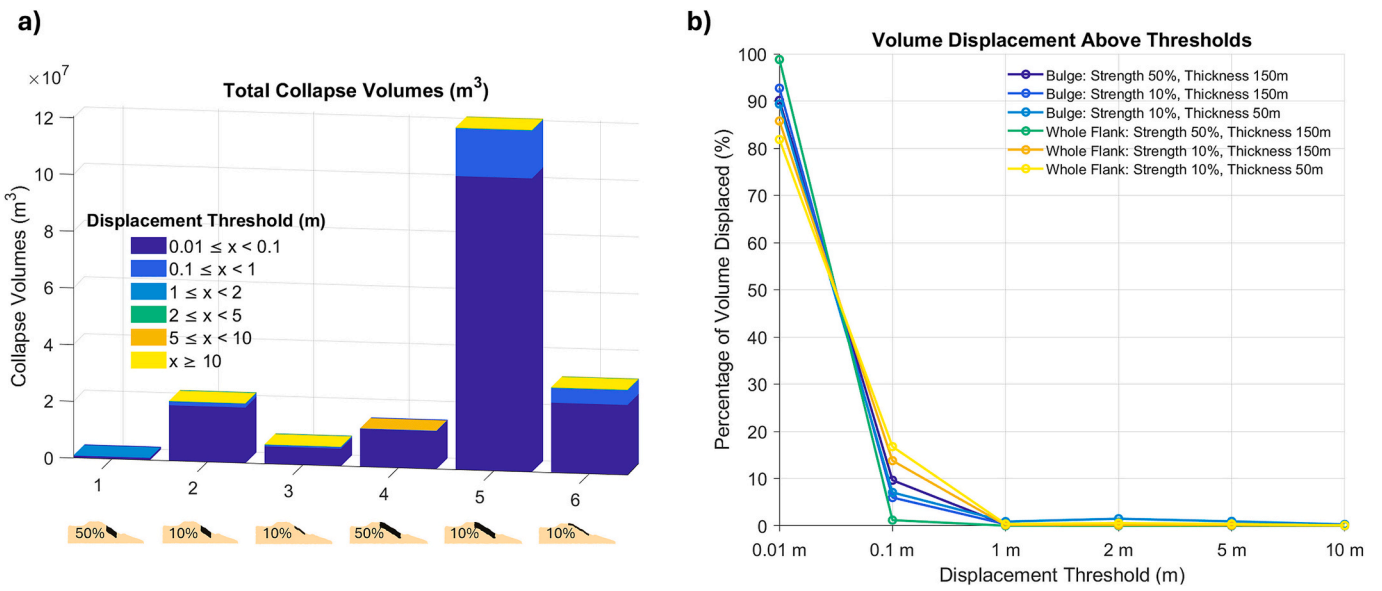

Fig. 8. Collapse volumes dgenerated from mechanical weakening using Discrete Element Method modelling. (a) shows a stacked bar chart representing the volume of material (m^3) displaced between thresholds in each model; (1):The Bulge: 50% Strength, 150 m Thickness, (2): The Bulge: 10% Strength, 150 m Thickness, (3): The Bulge: 10% Strength, 50 m Thickness, (4):Whole Flank: 50% Strength, 150 m Thickness, (5): Whole Flank: 10% Strength, 150 m Thickness, (6): Whole Flank: 10% Strength, 50 m Thickness. (b) shows the percentage of the total volume that displaced for each model between each threshold in each model.

2023a). Importantly, we see displacements towards the crest of the dome that fall outside the artificially weakened zone; this suggests that areas at risk of collapse are not confined to the bounds of the weakened zone. The areas of highest shear strain in all models typically correspond to the parts of the topography with the lowest rock strength and Young's modulus values. Our models show slumping in a retrogressive failure mechanism (increasing upslope). This has been seen in previous 2D models that incorporated a weakened hemispherical zone within an idealised near-hemispherical dome (Harnett et al., 2022).

The shear strain model scenarios typically show disaggregation at the surface, potentially due to a collapse downslope, such as the 2009 collapse scar at La Soufrière de Guadeloupe (Heap et al., 2021b). We note that several small-volume landslides occurred on the Chemin des Dames, a path on the west flank of the volcano, during Tropical Hurricane Fiona in September 2022. Small collapses such as these may indicate shallower, intense alteration. Indeed, Poganj et al. (2025) indicated the presence of altered rocks in some of the small-volume landslides that occurred in 2022. In both the models reduced to 50% and 10% of their original strength, detachment occurs at the crest of the dome, and disaggregation occurs downslope. Often, when there is a significant material contrast in a dome that is dipping downslope, it accentuates pre-existing planes of weakness and more shear strain accumulates (Harnett and Heap, 2021). Thus, this could give rise to the development of the detachment plane beneath the Bulge (Rosas-Carbajal et al., 2017, 2016). We also see curved planes beneath the subsurface that can be interpreted as developing rotational failure planes, where material is moving down and out of the southern slope.

Our results show that both the extent and distribution of hydrothermal alteration on the southern flank significantly impact displacement and failure behaviour. The southern flank (and the Bulge that lies within it) (Fig. 1) was a focus for our study, as it is the area where the greatest displacements are measured (Moretti et al., 2020; Rosas-Carbajal et al., 2017). Slope deformation and displacement is more prevalent in weaker hydrothermally altered rock (Heap et al., 2021b). When varying the spatial distribution of the alteration zones as seen in Fig. 5 and Fig. 6, we note that more significant displacement and shear strain occur when the weakened zone is larger. This aligns with previous modelling by Heap et al. (2021b), who found, using 2D FEM models, that the displacement of the southern flank increased when the size of the alteration zone was increased. A potential cause of the "patchy" disaggregation in Fig. 6c is the degree of heterogeneity within the model. Often, we see diffuse strain when the mechanical and geophysical properties in the model are uniform. We see that small or shallow weakened zones (Fig. 5 and Fig. 6 b-d) can still cause deep-seated, rotational displacements, which is crucial for the assessment of volcanic hazards. There is a higher risk for deformation and deep-seated rotational failure that leads to a rock avalanche when a weakened alteration zone is positioned on the flank (Darmawan et al., 2020; Harnett et al., 2022; Mueller et al., 2013).

5.2. *Choice of mechanical properties*

We use laboratory data provided by Heap et al. (2023a) to populate our models. The study of Heap et al. (2021b) showed that rocks with advanced argillic alteration promote reductions in UCS and Young's modulus. In their FEM stability models, these authors upscaled their laboratory data. The process of upscaling mechanical rock properties transforms measurements of rock behaviour (such as shear strength, deformation characteristics and elasticity) in the laboratory at a small scale (such as from a core sample) and extrapolates these measurements to a larger outcrop or edifice scale. Heap et al. (2021b) used the Geological Strength Index to upscale laboratory-derived Young's modulus, cohesion, internal friction values and Poisson's ratio values. The empirical fitting parameter m_i for the generalised Hoek-Brown failure criterion was calculated using the results of triaxial deformation experiments. The cohesion and internal friction angle were upscaled by transforming the generalised Hoek-Brown failure criterion to the Mohr-Coulomb failure criterion (Hoek et al., 2002). Overall, this upscaling significantly reduces the mechanical properties of the rocks, resulting in larger modelled displacements when compared to models that used laboratory-scale values (Heap et al., 2021b). In our study, we directly used the laboratory-scale data. If upscaling of mechanical parameters were performed for our models, we suggest the dome would likely show an increased level of instability. Thus, the models we show in this contribution are conservative estimates and, moreover, may underestimate potential hazard.

Heap et al. (2021b) created 2D models where lava domes were divided into discrete zones with homogeneous mechanical properties.

Three scenarios were considered: a homogeneous dome that is slightly or moderately altered; a weakened zone in the southern flank that is highly altered while the rest is slightly altered (similar to the altered zone we modelled from electrical tomography (Rosas-Carbajal et al., 2016)); and an artificially enlarged alteration zone where the entire southern flank is highly altered (a 2D setup that is also at a similar location to our 3D test scenarios). Models were run using both laboratory-scale and upscaled parameters for each. For their upscaled models, the shear strain and velocity rates were significantly higher than for the laboratory-scale models. By incorporating a weakened zone in their model, a sliding surface emerges in a similar location to where our models show detachment at the dome crest (Figs. 4 and 6). In our models, we observe smaller-scale rotational sliding planes (Fig. 4a-b), potentially due to the heterogeneity in our model, rather than one listric concave-upward structure. Fig. 4a suggests there is rotational failure of the material downslope. In their final scenario, Heap et al. (2021b) extend the altered zone to encompass the entire southern flank, reaching greater depths than the zone considered in this study (Fig. 5). This results in significantly increased shear strain rates and deformation compared to their other models, with surface velocities up to 0.05–0.1 mm/yr. Overall, both the findings in this study and in Heap et al. (2021b) indicate that hydrothermal alteration increases deformation and destabilises the dome. Heap et al. (2021b) suggest that their models underestimate surface deformation compared to the observed deformation of 0.3–0.7 cm/yr (Fig. 1; Moretti et al., 2020). This may be due to the homogeneous properties, the absence of structural features, and the 2D nature of the models limiting out-of-plane movement, and we emphasise the need for more complex, 3D approaches to capture the full scope of deformation at La Soufrière de Guadeloupe and at other volcanoes worldwide.

In addition, Heap et al. (2021b) previously generated a 3D strength map for the La Soufrière de Guadeloupe dome (similar to Fig. 2). Due to limited saturated data at the time of the study, they correlated uniaxial compressive strength (UCS) and wet bulk density values to create power-law functions, with UCS values up to 150 MPa. In contrast, we considered newly available UCS values, which peak at 131.3 MPa, as water lowers the strength of the rocks (Baud et al., 2000; C. Zhang et al., 2023). Thus, our models have a narrower range of strength parameters. While Heap et al. (2021b) acknowledges the uncertainty in the distribution of liquid-saturated and dry zones within La Soufrière de Guadeloupe, they opted to use wet bulk density, as it is more representative of a real volcanic system, particularly one of a volcano in a tropical climate. Thus, using the saturated data is also the approach we adopted. However, while Heap et al. (2021b) correlated their wet bulk density with UCS due to the dome summit being dry, we made our correlations with UCS. Research has shown that saturated domes typically exhibit larger displacements, though they may sometimes have smaller collapse volumes (Heap et al., 2023a). This suggests that the saturated nature of La Soufrière de Guadeloupe is an important factor influencing both displacement and collapse dynamics, and that perhaps in future studies, saturated (wet) and dry correlations could be compared. In addition, future analyses might determine which parts of the volcano are saturated and which parts are not, providing further modelling constraints.

Ball et al. (2018) demonstrated that models which neglect water saturation and permeability tend to overestimate both the collapse volume and the stability of the volcano. Our model therefore assumes a liquid-saturated dome. We clarify that we did not perform a coupled hydro-mechanical simulation (i.e., explicitly modelling pore fluid pressure or a dynamic water table). Instead, we simulate the mechanical consequence of saturation. By populating the low-density zones (identified via muon tomography) with liquid-saturated mechanical properties, the 'phreatic surface' in our model is effectively defined by the 3D boundaries of these zones. We rely on the interpretation by Rosas-Carbajal et al. (2016), which links these low-density regions to high-conductivity, liquid-saturated zones. This allows us to assess the stability impact of the weakened material in a conservative manner without introducing the complexity of a dynamic hydraulic model. A liquid-saturated dome also implies a larger gravitational loading than in a dry dome, as wet bulk density increases with water saturation, thus increasing the risk of hazard. Ball et al. (2018) use both 3D and 2D models to show that partially saturated domes with high pore-fluid pressures can reduce the factor of safety by up to 61% compared to dry domes. Thus, using parameters for dry volcanic rocks in our model would likely increase stability; however, this does not necessarily lead to larger collapse volumes. It is therefore critical to model more accurate dome saturation levels, permeability, and pore pressure to more comprehensively estimate collapse volumes and assess hazard.

5.3. Collapse volumes and runout modelling

Peruzzetto et al. (2019) modelled collapse volumes and corresponding debris avalanche runout scenarios for La Soufrière de Guadeloupe. They combined a 3D geometrical approach followed by numerical modelling using SHALTOP to simulate continuous and homogenous granular flow. They first highlight four regions with the potential to become a collapse volume (top A1 supremum, top A1 infimum, top A2 supremum, and top A2 infimum). These regions align detachment planes with subsurface conductive bodies (A1 and A2) to varied depths. The domain extents of these collapse volumes (from an aerial view along the x and y axes) are typically greater than in our collapse scenarios. The A1 scenario covers a region that is ~445 m wider than our southern flank model (Fig. 5c and supplementary Fig. S3c) along the x-axis. The A2 scenario is ~565 m wider on the x-axis, and both models are ~15 m longer along the y-axis than our southern flank scenario. The selected collapse volumes are on the southwest of the dome, rather than the exact south as in our models. The A1 and A2 collapse volumes are generated at similar depths below the surface to our models, and range from ~110–250 m. The collapse volumes calculated by Peruzzetto et al. (2019) range from 48–110$\times$ 10^6 m^3, which are larger than the collapse volumes we calculated at a 10 cm displacement threshold (Figs. 7 and 8). This is likely due to the selected collapse geometries being significantly larger than in our models. Our collapse volumes generated from the particles that moved over a 10 cm threshold range from 0.092 $\times$ 10^6 m^3 to 17.19 $\times$ 10^6 m^3. This is more in line with the final three scenarios from Peruzzetto et al. (2019). Three superficial scenarios (Dolomieu, South, and Southeast) were generated for unstable regions on the dome, with collapse volumes ranging from 1.10 $\times$ 10^6 m^3 to 9.70 $\times$ 10^6 m^3. The Dolomieu scenario extends from the left of the Bulge to the right of the southern flank scenario (centred more to the right of the dome). The South scenario is the most similar to our collapse volume extents and matches the length of our southern flank scenario (Fig. 5c). The South scenario stretches from the Lacroix fracture (on the eastern margin of our southern flank scenario) to a potential subsurface anomaly, aligning with features observed in our study. The Southeast scenario is to the right of the extent of our collapse volume. The final three superficial scenarios in Peruzzetto et al. (2019) have shallower depths (~50 m to 110 m) than their first four scenarios. Thus, these smaller collapse geometries lead to much smaller collapse volumes and are more like our models. In addition, the Bulge and southern flank models we generate are also superficial scenarios based on regions with alteration and potential planes of weakness.

To directly relate our collapse volume estimates for different alteration scenarios to hazard, we calculate the related debris avalanche runout distances using VolcFlow, using our collapse volumes as inputs. It is important to note that these calculations are performed whilst the debris avalanche remains on land (i.e., 100 s of flow). We do not consider the dynamics of the debris avalanche underwater as VolcFlow is intended to model subaerial flow. In Fig. 9, we present runout for the minimum (Fig. 9a and c) and maximum (Fig. 9b and d) collapse volumes determined from our DEM modelling.

The smallest collapse volume, which was generated in model 1 (see

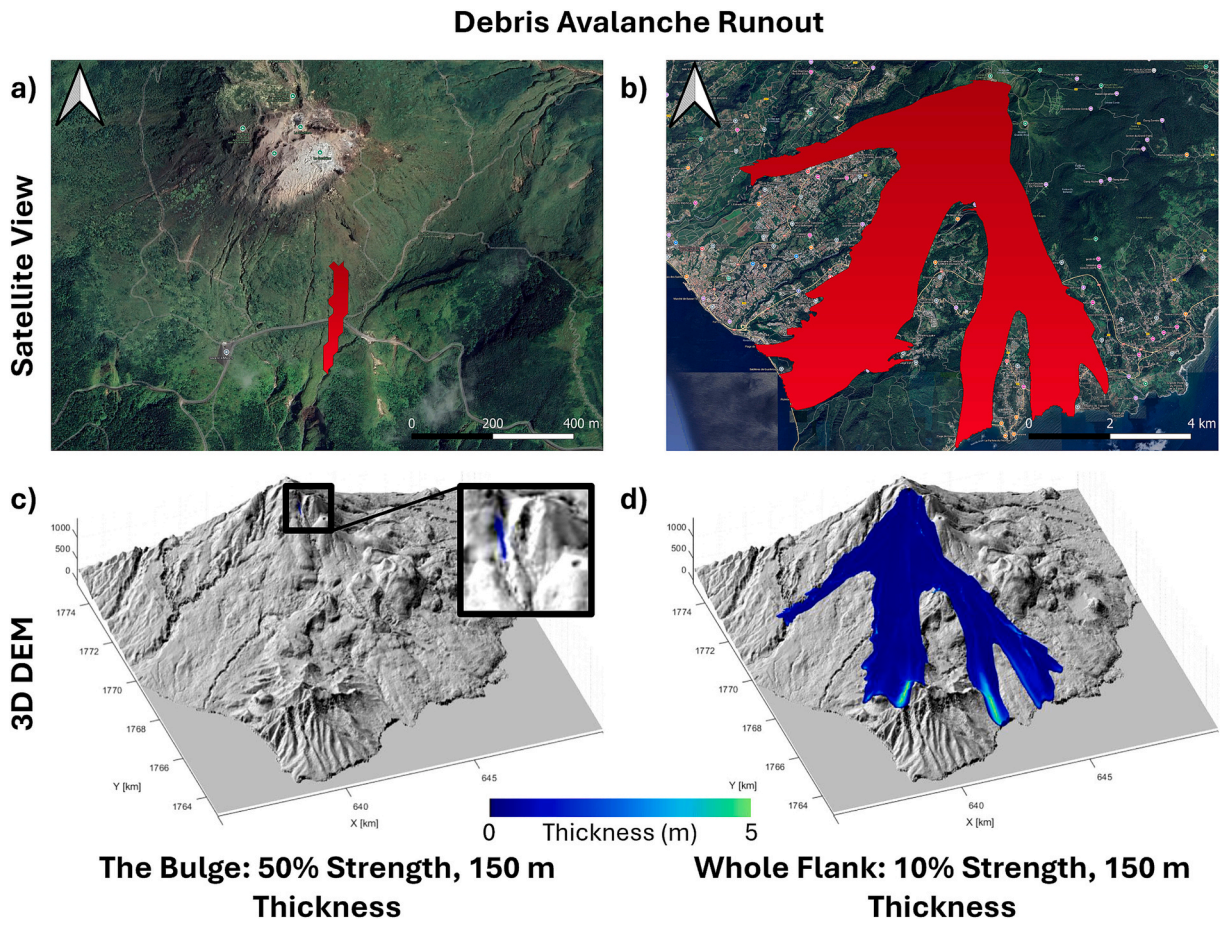

Fig. 9. Models showing the runout distances from the (a) and (c) model with the minimum (model 1), and (b) and (d) model with the maximum (model 5) debris avalanche volumes generated in VolcFlow, from collapse volumes generated in PFC. (a) and (b) show the runout on a hybrid satellite and terrain map, whilst (c) and (d) show the runout on the 3D DTM at $t = 100$ s. Basemap Data: Google, Landsat / Copernicus / ©2025 TerraMetrics / ©2025 Airbus / ©2025 Maxar Technologies / IBCAO.

Table 1), results in a modest flow, with a final average thickness of 0.49 m, and a significant final maximum thickness of 11.28 m. The maximum flow thickness during the debris avalanche was 19.52 m. For the range of average and maximum flow thicknesses throughout debris avalanche, see Supplementary Material Fig. S6. The maximum runout extends approximately 391 m downslope (Fig. 9a and c). The debris avalanche crosses a road, Route des Bains Jaunes, and thus would likely impact transport and tourism.

In contrast, the maximum collapse volume scenario (model 5, Fig. 9b and d), which was generated by reducing mechanical strength to 10% in the southern flank, shows a final average thickness of 0.52 m, and a final maximum thickness of 6.51 m. The final maximum thickness is significantly less in model 5 (largest collapse volume) than in model 1 (smallest collapse volume) (see Table 1). The comparison highlights a critical distinction in hazard impact: while larger volumes spread extensively to affect distal areas, material from smaller collapses remains concentrated. This results in substantial deposit thicknesses (>11 m) that pose a severe hazard of deep burial to proximal infrastructure (e.g., Route des Bains Jaunes), despite the shorter runout. The maximum flow thickness throughout the debris avalanche was at the beginning of the flow at 114.06 m. The average runout distance for this model is 8250.70 m and reaches the coast of Basse-Terre Island (Fig. 9 and supplementary Fig. S7). The towns of Saint-Claude and Trois-Rivières are affected by the flow. Historically, the La Soufrière de Guadeloupe dome has been associated with lateral explosions that trigger rock avalanches, which can travel distances of 1000 to 2000 m (Komorowski, 2005; Rosas-Carbajal et al., 2016). However, the 1530 CE eruption triggered a debris avalanche with runout distances from 9000 to 15,000 m.

Similar to VolcFlow, the SHALTOP model used by Peruzzetto et al. (2019) assumes a homogeneous avalanche and employs a depth-averaged approach. The model uses shallow-water equations and has been successfully applied to model rock avalanches and landslides (Kuo et al., 2009; Moretti et al., 2015; Peruzzetto et al., 2019). While Peruzzetto et al. (2019) maintain a constant collapse volume and vary the friction angle (using a Coulomb rheology), we tested a range of collapse volumes for different alteration scenarios, keeping the rheological yield strength constant (5000 Pa). This approach with constant reduction in stress allows us to isolate the effect of the initial collapse volume – driven by the alteration-induced instability modelled in PFC – on the final runout distance. Peruzzetto et al. (2019) found flow thicknesses at the top of the dome generally exceed 60 m, particularly for higher friction angles. This is equivalent to the flow thickness at the top of the dome for our maximum collapse volume scenario after approximately 10 s. In scenarios where the friction angle is less than 7°, the flow travels over 10,000 m, reaching the coast, similar to our maximum runout scenario. However, in cases where the friction angle exceeds 13°, the flow is more confined to the upper dome. When looking at the final three scenarios based on superficial geometries, we see the deposits are a lot thinner and less widespread. The South scenario of Peruzzetto et al. (2019) is most similar to our southern flank and Bulge models. For this South scenario, the flow does not exceed 20 m for friction angles <7° but still flows towards the town of Saint-Claude. Therefore, both our models and those of Peruzzetto et al. (2019) indicate that Saint-Claude is at risk.

5.4. The role of heterogeneity in modelling dome stability

Incorporating heterogeneity into volcanic dome modelling allows us to more accurately encapsulate their complex and heterogeneous nature. Previous studies, such as Heap et al. (2023b), found that incorporating rock heterogeneity is sufficient to compromise dome stability without any additional perturbing factors. Heap et al. (2023b) investigated the combined impact of heterogeneity and alteration on the stability of lava domes and found that the effects of diffuse heterogeneity are compounded when combined with discrete altered zones. These authors found that when the average strength of two domes was the same, the more heterogeneous dome was more prone to deformation and collapse. As we interpolate between our particles in PFC and the gridded geophysical data, we obtain continuous heterogeneous mechanical data for our full 3D model. Given the findings of Heap et al. (2023b), we therefore suggest our model is likely to provide more realistic displacement estimates than homogeneous models. Recently, field strength measurements highlighted that the dome at La Soufrière de Guadeloupe is characterised by a pronounced strength heterogeneity (Poganj et al., 2025). These authors found that not only do the strengths of rocks from different sites on the volcano vary significantly, but that the strengths of rocks from the same site also vary significantly. The findings of Poganj et al. (2025) support the need for incorporating material heterogeneity in volcano stability modelling.

To test the importance of heterogeneity in our models, we created a homogeneous model of the La Soufrière de Guadeloupe dome. To directly compare the model results, we re-ran one of the previous models (model 1 – weakening of the southern flank to 10% of its original strength at a thickness of 150 m – the scenario that showed maximum displacement) using a homogeneous dome instead of a heterogeneous dome. Fig. 10 compares results for the homogeneous (Fig. 10 a, b) dome and heterogeneous dome (Fig. 10 c, d). The homogeneous dome shows maximum displacements of 0.5 m. For the heterogeneous dome, we observe that the eastern side of the Bulge experiences the highest displacements, as this area is weaker than the rest of the dome. The maximum displacement in the heterogeneous model is 24 m. However, the homogeneous model shows a higher volume of material with displacements >10 cm (21.32×10^6 m^3) than the heterogeneous model (17.19×10^6 m^3). We suggest, therefore, that homogeneous models may both underestimate and overestimate displacements, depending on whether the homogeneous properties over- or underestimate the true mechanical properties within different parts of the dome. This suggests that incorporating heterogeneity is essential for accurate modelling, and that geophysical campaigns that allow us to quantify the subsurface heterogeneity are vital.

5.5. Vector comparison

To investigate the validity of the collapse scenarios modelled here, we compare the directions of our modelled displacement vectors to those of the GNSS velocity vectors (Fig. 1) (Moretti et al., 2020). We focus on a qualitative comparison of spatial patterns.

A comparison of the displacement vectors reveals a distinct spatial pattern. In the southern Bulge area, in the south of where we define an alteration zone in our models, the model successfully reproduces the southerly displacement direction observed in the GNSS data. This suggests that gravitational spreading of the weak, altered material is a primary driver of deformation in this specific sector. However, outside of this alteration zone, the model displacement vectors do not align with the GNSS observations. The discrepancy is expected and informative: it indicates that while alteration-induced gravitational instability may control deformation in the south, the broader deformation field recorded by GNSS across the rest of the dome is likely driven by processes not simulated in our gravity-driven model, such as deep-seated internal pressurisation or magmatic inflation. Therefore, the model effectively isolates the component of deformation attributable to alteration and gravity, distinguishing it from other volcanic processes.

The model setup is well settled and bonded before running our test scenarios. As a result, any significant displacement vectors are attributable to the weakening of an altered zone (such as the Bulge or the southern flank). Furthermore, most displacement vectors with displacement magnitudes exceeding the settled state occur either within or adjacent to these altered zones. Therefore, when comparing vector directions, we focus on the areas around the Bulge and the southern flank, where we can draw meaningful comparisons with the GNSS data.

We focussed on model 5 (Figs. 4c, 5c, and 7b) when comparing with

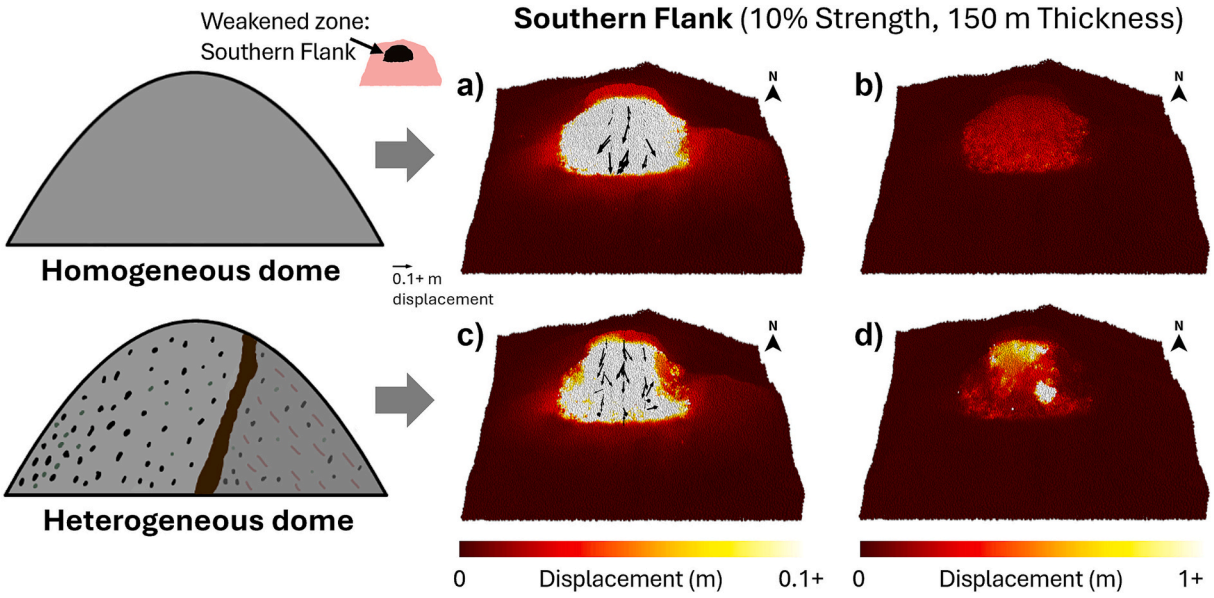

Fig. 10. Effect of material heterogeneity within our models. We show the results of performing the same weakening scenario on model 5 (reduction to 10% of the original bulk strength in the alteration zone at 150 m thickness on the southern flank) on both the (a)-(b) homogeneous and the (c)-(d) heterogeneous dome. We see the displacements on a 0 to >10 cm scale bar in (a) and (c), and displacements on a 0 to >1 m scale bar in (b) and (d). Displacement vectors are normalised and limited to a maximum magnitude of 0.1 m (10 cm). For visualisation purposes, vector lengths are scaled by a factor of 150. Thus, a plotted arrow length of 150 units represents a real displacement of at least 0.1 m.

the GNSS data, as model 5 shows the largest and clearest vector displacement patterns. We observe several key similarities between both patterns. Displacement vectors from the top of the dome extending southward, ending at the base of the southern flank alteration zone, follow a consistent southwestward trend, aligning well with GNSS velocity vector directions. South-southeast of the dome's centre, near the eastern edge of the Bulge region, the displacement vectors point south-southwest. This direction is slightly more southward than the southwest-orientated GNSS vectors in the same area. The vectors in this location are among the largest vectors seen in both the model and the GNSS data. Notably, this specific region consistently shows the most displacement across all model scenarios. This region is already mechanically weak, even before our alteration scenarios are applied, suggesting it may already represent a potential area of concern.

Additionally, once east of this weak region, the vectors shift direction and point southeast – another pattern that appears in the GNSS dataset. This directional change occurs particularly along the eastern edge of the Bulge and highlights a transition in deformation behaviour that both the model and GNSS data capture. One explanation for the directional change and the presence of larger displacement vectors is a shifting slope orientation of the dome in combination with the weaker, altered material.

Displacements elsewhere on the model, which are several orders of magnitude smaller due to the model settling, are inward-directed owing to the compaction induced by the reduction of material modulus concomitant with weakening. This could be interpreted to mean that processes other than alteration-induced weakening, such as pore fluid pressurisation or sliding on a décollement, which are not accounted for in our models, are additional components to the mainly outward-directed horizontal displacement field observed in GNSS data across the dome.

5.6. Subsurface alteration

Previous electrical conductivity surveys conducted on La Soufrière de Guadeloupe by Rosas-Carbajal et al. (2016) identified zones of high electrical conductivity, which are interpreted as hydrothermally altered regions beneath the surface of the southern flank. The largest conductive region, the A1 anomaly, is located in the southern flank and contains a sub-region, the A2 anomaly, with values of even higher conductivity (>1 Siemens) (Rosas-Carbajal et al., 2016). The overall anomaly is a concave upward listric structure that starts below the summit of the dome, curves beneath the Bulge, and surfaces in the south. The A1 anomaly is interpreted as moderately altered, whilst the A2 anomaly it encompasses is relatively higher in conductivity and interpreted as highly altered.

Although the muon data only extends to a depth of approximately 1300 m – considerably shallower than the full extent of the listric structure (see Rosas-Carbajal et al., 2016, Supplementary Fig. S21) – our objective is to model the effects of mechanical weakening in this structure as accurately as possible (within the limitations of our model). We do this to explore the potential implications of further hydrothermal alteration within the moderately altered region. In particular, we examine the effects of extending the characteristics of the highly altered A2 anomaly into the surrounding moderately altered areas of the A1 anomaly. Thus, we can assess possible outcomes of intensified hydrothermal activity in zones currently classified as only moderately altered. We weakened this zone (A1 and A2 anomaly inclusive) to 10% of its original strength, as in our other models (see Figs. 3 and 5). However, as the location of the bottom part of these anomalies lie outside the range of our geophysical data, the bottom section consists of homogeneous material (the average modal values selected) and does not incorporate any previously weakened zones. The spatial extent of this listric structure follows the width and location of the Bulge weakened zone (as the Bulge lies above the anomaly) and is 172 m thick. It lies at minimum and maximum depths of approximately 55 m and 175 m below the surface, respectively.

Initially, we see that the surface displacements are smaller in magnitude than in our previous models with shallower-seated weakening. This may be because the weakened listric zone lies deeper in the subsurface, where the data is predominantly homogeneous. However, the maximum displacement in the model is 3 m. Therefore, although this is the lowest maximum displacement of our models reduced to 10% strength, sufficient material has been displaced to qualify for our collapse volume threshold. The highest displacements occur 70 m (Fig. 11a) below the roof of the dome. Displacements in this location could be described as slumping due to an internal weakened zone, with displacement vectors pointing vertically downward. This is in line with the 2D models presented in Harnett et al. (2022), as well as with prior 3D proof-of-concept models we developed exploring the effect of internal weakened zones in three dimensions.

When comparing with the GNSS patterns (Moretti et al., 2020), we observe a west-southwestward trend in displacement on the right edge of the topography above the conductive region discussed in Rosas-Carbajal et al. (2016). (underlying). This trend is slightly more westward than the GNSS vectors, suggesting that increased rock weakening, such as alteration, may lead to a greater westward deflection in displacement direction. In contrast to our other models, north of the dome and on the east side of the weakened listric structure, some displacement vectors trend northward. These vectors dip into the subsurface at approximately 45 degrees, with horizontal components pointing north (Fig. 11b). However, the majority of these displacements are small (2–3 mm) and occur within the subsurface, originating at the bottom of the listric structure at the north end. On the west side of the listric structure, also north of the dome, vectors show a southward trend, moving downslope with the rest of the flank. The contrast suggests that the northeastern part of the dome is comparatively more stable or more biased towards northward displacement.

Overall, the displacements in the model shown in Fig. 11 are larger on the west of the southern flank (Fig. 11a), from the top of the dome to

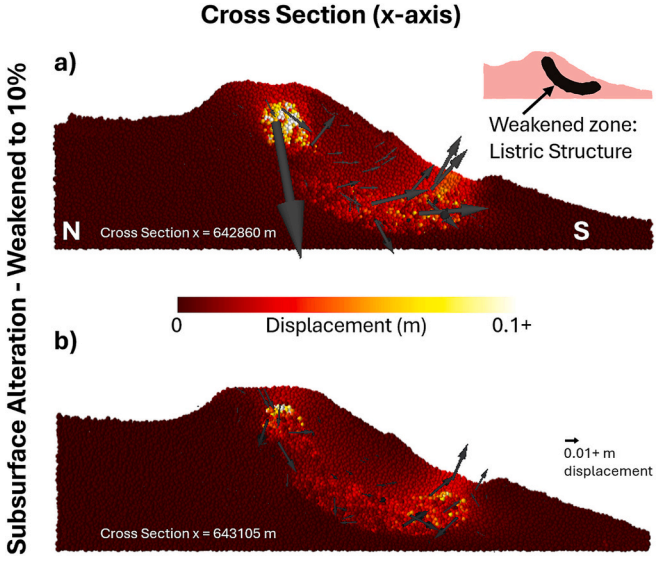

Fig. 11. We show the results of weakening a concave upward listric structure (reduction to 10% of the original bulk strength) within the subsurface that represents a region with high electrical conductivity values in Rosas-Carbajal et al. (2016). Panels (a) and (b) display parallel cross-sections positioned approximately at the western and eastern boundaries of the Bulge, respectively. This spacing (~200 m) captures the variability of deformation across the southern flank. Panel (a) corresponds to the western bound, while (b) corresponds to the eastern bound. Displacement vectors are normalised and limited to a maximum magnitude of 0.1 m (10 cm). For visualisation purposes, vector lengths are scaled by a factor of 500. Thus, a plotted arrow length of 500 units represents a real displacement of at least 0.1 m.

the bottom of the slope. There are consistent displacements along the base of the slope on the southern flank. In our previous models (Figs. 3 and 5), the biggest displacements were on the east of the southern flank, at the eastern edge of the Bulge. This difference arises because our previous models simulated extensive weakening of the shallower dome and summit region. In contrast, the current scenario restricts weakening to the deep listric structure, preserving the original, higher strength of the overlying shallower rock. Consequently, deformation is governed by the mechanics of the deep subsurface rather than surface-level instability. In addition, analysis of the geophysical input suggests that the high-density region below 1300 m is likely artificial. Rosas-Carbajal et al. (2017) note that muon coverage is limited below this altitude, as the region was resolvable by only one telescope site. In our input density model, this zone exhibits linear, geometric density boundaries that appear to represent the limits of the inversion grid rather than resolved geological structures. Consequently, the correlated UCS values in our model are likely artificially high within this listric weakened zone. Moreover, due to the lack of heterogeneity outside the bound of the muon data as the depth increases, our displacement estimations are likely conservative and indicate that further alteration of these regions should be closely monitored.

5.7. Applicability in other contexts

The discrete element method (DEM) used here is transferable to a range of modelling approaches and contexts. While similar weakening models are possible using finite element methods (FEM), the DEM offers advantages (Section 3.1) when dealing with large displacements and complex strain patterns, such as those occurring in extensive volcanic edifices and flank failures. For large-strain problems where we are looking at volumes displacing >10 cm, the use of DEM is advantageous. The use of FEM may be particularly complementary for time-dependent displacement analysis (i.e., to compare yearly displacement rates).

The approach demonstrated here requires a DTM of the desired location and some values for key input parameters; it can then be applied to volcanoes worldwide. The model does not require fully heterogeneous data; in its absence, a simplified homogeneous or artificially heterogeneous model (i.e., created using a Weibull probability function (Heap et al., 2023b; Tang, 1997; Tang and Tang, 2011; Wong et al., 2006)) can still yield useful results.

The workflow begins with a DTM, followed by interpolation of mechanical and/or geophysical parameters to correlate with model elements. We then apply weakening to predefined alteration zones, varying the degree, thickness, and spatial extent as needed.

6. Conclusions

In this study, we developed a novel 3D modelling approach to examine the impact of hydrothermal alteration on the stability of volcanic domes, using the La Soufrière de Guadeloupe lava dome as a case study. We visualise displacement as well as perform novel 3D finite shear strain modelling for various mechanical weakening scenarios. Our findings show that alteration-induced weakening significantly increases displacement and instability within the dome, even in regions surrounding the zones directly affected by alteration. We also demonstrate that varying the spatial extent of the weakened zone produces different displacement patterns, which allows for a more precise identification of high-risk areas: the most hazardous scenarios are observed when the entire southern flank of La Soufrière de Guadeloupe undergoes alteration. Shallow mechanically weakened zones (50 m in depth) can lead to deep-seated displacements hundreds of metres into the subsurface. In our strain models, we observe a characteristic failure pattern in which the material deforms progressively along angled, planar detachments – consistent with delamination through shear fracture propagation. Such patterns suggest that alteration-induced weakening can promote gradual, stepwise collapse, rather than sudden failure. By quantifying collapse volumes generated by alteration-related deformation, we estimate potential debris flow runout distances. The minimum collapse volume modelled here is 0.092×10^6 m^3, which generates a runout distance of 391 m, whilst the maximum collapse volume modelled here is 17.19×10^6 m^3, which generates a runout distance of 8250 m. Therefore, we conclude that alteration increases both the size of the collapse volume and runout distance of debris avalanches. We suggest that using geophysical data to incorporate rock heterogeneity into our models improves collapse volume and runout distance predictions. These results highlight the critical importance of considering both heterogeneity and hydrothermal alteration when forecasting volcanic hazards. Our approach provides a comprehensive framework for linking rock weakening (via hydrothermal alteration) to collapse dynamics, offering valuable insights for future research and real-world hazard assessments.

CRediT authorship contribution statement

K.D. Ní Nualláin: Writing – review & editing, Writing – original draft, Visualization, Software, Resources, Project administration, Methodology, Investigation, Funding acquisition, Formal analysis, Data curation, Conceptualization. **C.E. Harnett:** Writing – review & editing, Supervision, Resources, Funding acquisition, Conceptualization. **A. Hrysiewicz:** Writing – review & editing, Visualization, Formal analysis, Data curation. **M.J. Heap:** Writing – review & editing, Data curation. **T. R. Walter:** Writing – review & editing, Data curation. **M. Rosas-Carbajal:** Writing – review & editing, Data curation.

Declaration of competing interest

The authors declare that they have no known competing financial interests or personal relationships that could have appeared to influence the work reported in this paper.

Acknowledgements

KDN acknowledges receipt of Taighde Éireann – Research Ireland funding under the Government of Ireland Postgraduate Scholarship Programme (GOIPG/2022/1904 and GOIPG/2024/4500). KDN, CEH, MJH and TRW were supported by ROTTnROCK, a research project funded by the European Research Council under the European Union's Horizon Europe Programme / ERC Synergy grant (ERC-2023-SyG 101118491). CEH acknowledges funding from iCRAG, the Research Ireland Centre in Applied Geosciences (iCRAG-Phase 2 – Grand Code: 13/RC/2092_P2). AH acknowledges the ESA Living Planet Fellowship (Grant Code: 4000139950/22/I-DT-lr), received during the study period, as Eoghan P. Holohan as mentor. MJH was additionally supported by ANR grant MYGALE ("Modelling the phYsical and chemical Gradients of hydrothermal ALteration for warning systems of flank collapse at Explosive volcanoes"; ANR-21-CE49-0010) and the Institut Universitaire de France (IUF). We also thank Wessel et al. (2019) for the development and availability of GMT6 used to create certain figures of this manuscript. The TanDEM-X Digital Elevation Model were provided by the German Aerospace Center (DLR proposal ID thomwal_DEM_GEOL3419). Finally, we gracefully thank the VolcFlow's authors for the availability of their software to the community.

Appendix A. Supplementary data

Supplementary data to this article can be found online at https://doi.org/10.1016/j.jvolgeores.2026.108566.

Data availability

The visualisation code is available at: 10.5281/zenodo.18230722.

References

Alvarez-Fernandez, M.I., Amor-Herrera, E., Gonzalez-Nicieza, C., Lopez-Gayarre, F., Avial-Llardent, M.R., 2013. Forensic analysis of the instability of a large-scale slope in a coal mining operation. Eng. Fail. Anal. 33, 197–211. https://doi.org/10.1016/j.engfailanal.2013.05.001.

Archie, G.E., 1942. The electrical resistivity log as an Aid in determining some reservoir characteristics. Trans. AIME 146, 54–62. https://doi.org/10.2118/942054-G.

Ashwell, P.A., Kennedy, B.M., Edwards, M., Cole, J.W., 2018. Characteristics and consequences of lava dome collapse at Ruawahia, Taupo Volcanic Zone, New Zealand. Bull. Volcanol. 80, 43. https://doi.org/10.1007/s00445-018-1217-1.

Ball, J.L., Calder, E.S., Hubbard, B.E., Bernstein, M.L., 2013. An assessment of hydrothermal alteration in the Santiaguito lava dome complex, Guatemala: implications for dome collapse hazards. Bull. Volcanol. 75, 676. https://doi.org/10.1007/s00445-012-0676-z.

Ball, J.L., Stauffer, P.H., Calder, E.S., Valentine, G.A., 2015. The hydrothermal alteration of cooling lava domes. Bull. Volcanol. 77, 102. https://doi.org/10.1007/s00445-015-0986-z.

Ball, J.L., Taron, J., Reid, M.E., Hurwitz, S., Finn, C., Bedrosian, P., 2018. Combining multiphase groundwater flow and slope stability models to assess stratovolcano flank collapse in the Cascade Range. J. Geophys. Res. Solid Earth 123, 2787–2805. https://doi.org/10.1002/2017JB015156.

Barde-Cabusson, S., Bolós, X., Pedrazzi, D., Lovera, R., Serra, G., Martí, J., Casas, A., 2013. Electrical resistivity tomography revealing the internal structure of monogenetic volcanoes. Geophys. Res. Lett. 40, 2544–2549. https://doi.org/10.1002/grl.50538.

Bardou, E., Bowen, P., Banfill, P.G., Boivin, P., 2004. Dramatical Impact of Low Amounts of Swelling Clays on the Rheology of Alpine Debris Flows. Presented at the AGU Fall Meeting Abstracts, pp. H41B-0293.

Bardou, E., Bowen, P., Boivin, P., Banfill, P., 2007. Impact of small amounts of swelling clays on the physical properties of debris-flow-like granular materials. Implications for the study of alpine debris flow. Earth Surf. Process. Landf. 32, 698–710. https://doi.org/10.1002/esp.1412.

Baud, P., Zhu, W., Wong, T., 2000. Failure mode and weakening effect of water on sandstone. J. Geophys. Res. Solid Earth 105, 16371–16389. https://doi.org/10.1029/2000JB900087.

Boichu, M., Villemant, B., Boudon, G., 2008. A model for episodic degassing of an andesitic magma intrusion. J. Geophys. Res. Solid Earth 113. https://doi.org/10.1029/2007JB005130.

Boudon, G., Le Friant, A., Komorowski, J.-C., Deplus, C., Semet, M.P., 2007. Volcano flank instability in the Lesser Antilles Arc: diversity of scale, processes, and temporal recurrence. J. Geophys. Res. Solid Earth 112. https://doi.org/10.1029/2006JB004674.

Bourgouin, L., Mühlhaus, H.-B., Jane Hale, A., Arsac, A., 2007. Studying the influence of a solid shell on lava dome growth and evolution using the level set method. Geophys. J. Int. 170, 1431–1438. https://doi.org/10.1111/j.1365-246X.2007.03471.x.

Cabrera-Pérez, I., Soubestre, J., D'Auria, L., van Dorth, D.M., Ledo, J., Piña-Varas, P., Cervigón-Tomico, G., Padilla, G.D., Barrancos, J., Pérez, N.M., 2023. Ambient noise tomography of Gran Canaria island (Canary Islands) for geothermal exploration. Geothermics 108, 102609. https://doi.org/10.1016/j.geothermics.2022.102609.

Cabrera-Pérez, I., D'Auria, L., Soubestre, J., del Pezzo, E., Prudencio, J., Ibáñez, J.M., Jiménez-Mejías, M., Padilla, G.D., Barrancos, J., Pérez, N.M., 2024. 3-D intrinsic attenuation tomography using ambient seismic noise applied to La Palma Island (Canary Islands). Sci. Rep. 14, 27354. https://doi.org/10.1038/s41598-024-79076-w.

Cai, M., 2010. Practical estimates of tensile strength and Hoek–Brown strength parameter mi of brittle rocks. Rock Mech. Rock. Eng. 43, 167–184. https://doi.org/10.1007/s00603-009-0053-1.

Calder, E.S., Luckett, R., Sparks, R.S.J., Voight, B., 2002. Mechanisms of lava dome instability and generation of rockfalls and pyroclastic flows at Soufrière Hills Volcano, Montserrat. Geol. Soc. Lond. Mem. 21, 173–190. https://doi.org/10.1144/GSL.MEM.2002.021.01.08.

Calder, E.S., Lavallée, Y., Kendrick, J.E., Bernstein, M., 2015. Chapter 18 - Lava dome eruptions. In: Sigurdsson, H. (Ed.), The Encyclopedia of Volcanoes, Second edition. Academic Press, Amsterdam, pp. 343–362. https://doi.org/10.1016/B978-0-12-385938-9.00018-3.

Cardozo, N., Allmendinger, R.W., 2009. SSPX: a program to compute strain from displacement/velocity data. Comput. Geosci. 35, 1343–1357. https://doi.org/10.1016/j.cageo.2008.05.008.

Carn, S.A., Watts, R.B., Thompson, G., Norton, G.E., 2004. Anatomy of a lava dome collapse: the 20 March 2000 event at Soufrière Hills Volcano, Montserrat. J. Volcanol. Geotherm. Res. 131, 241–264. https://doi.org/10.1016/S0377-0273(03)00364-0.

Castro-Melgar, I., Prudencio, J., Del Pezzo, E., Giampiccolo, E., Ibáñez, J.M., 2021. Shallow magma storage beneath Mt. Etna: evidence from new attenuation tomography and existing velocity models. J. Geophys. Res. Solid Earth 126, e2021JB022094. https://doi.org/10.1029/2021JB022094.

Cundall, P.A., Strack, O.D.L., 1979. A discrete numerical model for granular assemblies. Géotechnique 29, 47–65. https://doi.org/10.1680/geot.1979.29.1.47.

Darmawan, H., Yuliantoro, P., Rakhman, A., Budi Santoso, A., Humaida, H., Suryanto, W., 2020. Dynamic velocity and seismic characteristics of gravitational rockfalls at the Merapi lava dome. J. Volcanol. Geotherm. Res. 404, 107010. https://doi.org/10.1016/j.jvolgeores.2020.107010.

Darmawan, H., Troll, V.R., Walter, T.R., Deegan, F.M., Geiger, H., Heap, M.J., Seraphine, N., Harris, C., Humaida, H., Müller, D., 2022. Hidden mechanical weaknesses within lava domes provided by buried high-porosity hydrothermal alteration zones. Sci. Rep. 12, 3202. https://doi.org/10.1038/s41598-022-06765-9.

de van Vries, B.W., Kerle, N., Petley, D., 2000. Sector collapse forming at Casita volcano, Nicaragua. Geology 28, 167–170. https://doi.org/10.1130/0091-7613(2000)28<167:SCFACV>2.0.CO;2.

del Potro, R., Hürlimann, M., 2009. The decrease in the shear strength of volcanic materials with argillic hydrothermal alteration, insights from the summit region of Teide stratovolcano, Tenerife. Eng. Geol. 104, 135–143. https://doi.org/10.1016/j.enggeo.2008.09.005.

Diefenbach, A.K., Bull, K.F., Wessels, R.L., McGimsey, R.G., 2013. Photogrammetric monitoring of lava dome growth during the 2009 eruption of Redoubt Volcano. J. Volcanol. Geotherm. Res. 259, 308–316. https://doi.org/10.1016/j.jvolgeores.2011.12.009. The 2009 Eruption of Redoubt Volcano, Alaska.

Farr, T.G., Rosen, P.A., Caro, E., Crippen, R., Duren, R., Hensley, S., Kobrick, M., Paller, M., Rodriguez, E., Roth, L., Seal, D., Shaffer, S., Shimada, J., Umland, J., Werner, M., Oskin, M., Burbank, D., Alsdorf, D., 2007. The shuttle radar topography mission. Rev. Geophys. 45. https://doi.org/10.1029/2005RG000183.

Feuillard, M., Allegre, C.J., Brandeis, G., Gaulon, R., Le Mouel, J.L., Mercier, J.C., Pozzi, J.P., Semet, M.P., 1983. The 1975–1977 crisis of la Soufriere de Guadeloupe (F.W.I): a still-born magmatic eruption. J. Volcanol. Geotherm. Res. 16, 317–334. https://doi.org/10.1016/0377-0273(83)90036-7.

Finn, C.A., Deszcz-Pan, M., Ball, J.L., Bloss, B.J., Minsley, B.J., 2018. Three-dimensional geophysical mapping of shallow water saturated altered rocks at Mount Baker, Washington: implications for slope stability. J. Volcanol. Geotherm. Res. 357, 261–275. https://doi.org/10.1016/j.jvolgeores.2018.04.013.

Friant, A.L., Boudon, G., Komorowski, J.-C., Heinrich, P., Semet, M.P., 2006. Potential flank-collapse of Soufrière Volcano, Guadeloupe, Lesser Antilles? Numerical simulation and hazards. Nat. Hazards 39, 381–393. https://doi.org/10.1007/s11069-005-6128-8.

Gago, F., Mužík, J., Bulko, R., 2019. The slope stability solution using meshless local Petrov-Galerkin method. In: Transp. Res. Procedia, TRANSCOM 2019 13th International Scientific Conference on Sustainable, Modern and Safe Transport, 40, pp. 686–693. https://doi.org/10.1016/j.trpro.2019.07.097.

Hale, A.J., 2008. Lava dome growth and evolution with an independently deformable talus. Geophys. J. Int. 174, 391–417. https://doi.org/10.1111/j.1365-246X.2008.03806.x.

Hale, A.J., Wadge, G., 2008. The transition from endogenous to exogenous growth of lava domes with the development of shear bands. J. Volcanol. Geotherm. Res. 171, 237–257. https://doi.org/10.1016/j.jvolgeores.2007.12.016.

Hale, A.J., Calder, E.S., Loughlin, S.C., Wadge, G., Ryan, G.A., 2009a. Modelling the lava dome extruded at Soufrière Hills Volcano, Montserrat, August 2005–May 2006: part II: rockfall activity and talus deformation. J. Volcanol. Geotherm. Res. 187, 69–84. https://doi.org/10.1016/j.jvolgeores.2009.08.014.

Hale, A.J., Calder, E.S., Wadge, G., Loughlin, S.C., Ryan, G.A., 2009b. Modelling the lava dome extruded at Soufrière Hills Volcano, Montserrat, August 2005–May 2006: part I: dome shape and internal structure. J. Volcanol. Geotherm. Res. 187, 53–68. https://doi.org/10.1016/j.jvolgeores.2009.08.023.

Harnett, C.E., 2019. Understanding the Mechanics of Lava Dome Collapse (Phd). University of Leeds.

Harnett, C.E., Heap, M.J., 2021. Mechanical and topographic factors influencing lava dome growth and collapse. J. Volcanol. Geotherm. Res. 420, 107398. https://doi.org/10.1016/j.jvolgeores.2021.107398.

Harnett, C.E., Thomas, M.E., Purvance, M.D., Neuberg, J., 2018. Using a discrete element approach to model lava dome emplacement and collapse. J. Volcanol. Geotherm. Res. 359, 68–77. https://doi.org/10.1016/j.jvolgeores.2018.06.017.

Harnett, C.E., Kendrick, J.E., Lamur, A., Thomas, M.E., Stinton, A., Wallace, P.A., Utley, J.E.P., Murphy, W., Neuberg, J., Lavallée, Y., 2019. Evolution of mechanical properties of Lava Dome Rocks across the 1995–2010 Eruption of Soufrière Hills Volcano, Montserrat. Front. Earth Sci. 7. https://doi.org/10.3389/feart.2019.00007.

Harnett, C.E., Heap, M.J., Thomas, M.E., 2020. A toolbox for identifying the expression of dome-forming volcanism on exoplanets. Planet. Space Sci. 180, 104762. https://doi.org/10.1016/j.pss.2019.104762.

Harnett, C.E., Heap, M.J., Troll, V.R., Deegan, F.M., Walter, T.R., 2022. Large-scale lava dome fracturing as a result of concealed weakened zones. Geology 50, 1346–1350. https://doi.org/10.1130/G50396.1.

He, M.C., Feng, J.L., Sun, X.M., 2008. Stability evaluation and optimal excavated design of rock slope at Antaibao open pit coal mine, China. Int. J. Rock Mech. Min. Sci. 45, 289–302. https://doi.org/10.1016/j.ijrmms.2007.05.007.

Heap, M.J., Baumann, T., Gilg, H.A., Kolzenburg, S., Ryan, A.G., Villeneuve, M., Russell, J.K., Kennedy, L.A., Rosas-Carbajal, M., Clynne, M.A., 2021a. Hydrothermal alteration can result in pore pressurization and volcano instability. Geology 49, 1348–1352. https://doi.org/10.1130/G49063.1.

Heap, M.J., Baumann, T.S., Rosas-Carbajal, M., Komorowski, J.-C., Gilg, H.A., Villeneuve, M., Moretti, R., Baud, P., Carbillet, L., Harnett, C., Reuschlé, T., 2021b. Alteration-induced volcano instability at La Soufrière de Guadeloupe (Eastern Caribbean). J. Geophys. Res. Solid Earth 126, e2021JB022514. https://doi.org/10.1029/2021JB022514.

Heap, M.J., Harnett, C.E., Wadsworth, F.B., Gilg, H.A., Carbillet, L., Rosas-Carbajal, M., Komorowski, J.-C., Baud, P., Troll, V.R., Deegan, F.M., Holohan, E.P., Moretti, R., 2022. The tensile strength of hydrothermally altered volcanic rocks. J. Volcanol. Geotherm. Res. 428, 107576. https://doi.org/10.1016/j.jvolgeores.2022.107576.

Heap, M.J., Harnett, C., Farquharson, J., Baud, P., Rosas-Carbajal, M., Komorowski, J.-C., Violay, M.E.S., Gilg, H.A., Reuschlé, T., 2023a. The influence of water-saturation on the strength of volcanic rocks and the stability of lava domes. J. Volcanol. Geotherm. Res. 444, 107962. https://doi.org/10.1016/j.jvolgeores.2023.107962.

Heap, M.J., Harnett, C.E., Nazarbayov, T., Heng, Z., Baud, P., Xu, T., Rosas-Carbajal, M., Komorowski, J.-C., 2023b. The influence of heterogeneity on the strength of volcanic rocks and the stability of lava domes. Bull. Volcanol. 85, 49. https://doi.org/10.1007/s00445-023-01669-6.

Hoek, E., Carranza-Torres, C., Corkum, B., 2002. Hoek-Brown failure criterion-2002 edition. Proc. NARMS-Tac 1, 267–273.

Holohan, E.P., Schöpfer, M.P.J., Walsh, J.J., 2015. Stress evolution during caldera collapse. Earth Planet. Sci. Lett. 421, 139–151.

Huppert, H.E., Shepherd, J.B., Haraldur Sigurdsson, R., Sparks, S.J., 1982. On lava dome growth, with application to the 1979 lava extrusion of the Soufrière of St. Vincent. J. Volcanol. Geotherm. Res. 14, 199–222. https://doi.org/10.1016/0377-0273(82)90062-2.

Husain, T., Elsworth, D., Voight, B., Mattioli, G., Jansma, P., 2019. Morphologic variation of an evolving dome controlled by the extrusion of finite yield strength magma. J. Volcanol. Geotherm. Res. 370, 51–64. https://doi.org/10.1016/j.jvolgeores.2019.01.010.

Hutchison, W., Varley, N., Pyle, D.M., Mather, T.A., Stevenson, J.A., 2013. Airborne thermal remote sensing of the Volcán de Colima (Mexico) lava dome from 2007 to 2010. Geol. Soc. Lond. Spec. Publ. 380, 203–228. https://doi.org/10.1144/SP380.8.

Jessop, D.E., Moune, S., Moretti, R., Gibert, D., Komorowski, J.-C., Robert, V., Heap, M.J., Bosson, A., Bonifacie, M., Deroussi, S., Dessert, C., Rosas-Carbajal, M., Lemarchand, A., Burtin, A., 2021. A multi-decadal view of the heat and mass budget of a volcano in unrest: La Soufrière de Guadeloupe (French West Indies). Bull. Volcanol. 83, 16. https://doi.org/10.1007/s00445-021-01439-2.

Jiang, Y.S., Zimmermann, Th., 1992. Indirect boundary element algorithm for slope stability analysis. Eng. Anal. Bound. Elem. 9, 209–217. https://doi.org/10.1016/0955-7997(92)90095-O.

John, D.A., Sisson, T.W., Breit, G.N., Rye, R.O., Vallance, J.W., 2008. Characteristics, extent and origin of hydrothermal alteration at Mount Rainier Volcano, Cascades Arc, USA: implications for debris-flow hazards and mineral deposits. J. Volcanol. Geotherm. Res. 175, 289–314. https://doi.org/10.1016/j.jvolgeores.2008.04.004.

Kelfoun, K., Vallejo Vargas, S., 2016. VolcFlow capabilities and potential development for the simulation of lava. Geol. Soc. Lond. Spec. Publ. 426, 337–343. https://doi.org/10.1144/SP426.8.

Kelfoun, K., Samaniego, P., Palacios, P., Barba, D., 2009. Testing the suitability of frictional behaviour for pyroclastic flow simulation by comparison with a well-constrained eruption at Tungurahua volcano (Ecuador). Bull. Volcanol. 71, 1057–1075. https://doi.org/10.1007/s00445-009-0286-6.

Kendrick, J.E., Schaefer, L.N., Schauroth, J., Bell, A.F., Lamb, O.D., Lamur, A., Miwa, T., Coats, R., Lavallée, Y., Kennedy, B.M., 2021. Physical and mechanical rock properties of a heterogeneous volcano: the case of Mount Unzen, Japan. Solid Earth 12, 633–664. https://doi.org/10.5194/se-12-633-2021.

Kereszturi, G., Lauren, Schaefer, Stuart, Mead, Craig, Miller, Jonathan, Procter, Kennedy, B., 2021. Synthesis of hydrothermal alteration, rock mechanics and geophysical mapping to constrain failure and debris avalanche hazards at Mt. Ruapehu (New Zealand). N. Z. J. Geol. Geophys. 64, 421–442. https://doi.org/10.1080/00288306.2021.1885048.

Komorowski, J.-C., 2005. Volcanic hazard atlas of the lesser antilles. Ch Guadeloupe 65–102.

Kuo, C.Y., Tai, Y.C., Bouchut, F., Mangeney, A., Pelanti, M., Chen, R.F., Chang, K.J., 2009. Simulation of Tsaoling landslide, Taiwan, based on Saint Venant equations over general topography. Eng. Geol. 104, 181–189. https://doi.org/10.1016/j.enggeo.2008.10.003.

Lesparre, N., Gibert, D., Marteau, J., Komorowski, J.-C., Nicollin, F., Coutant, O., 2012. Density muon radiography of La Soufrière of Guadeloupe volcano: comparison with geological, electrical resistivity and gravity data. Geophys. J. Int. 190, 1008–1019. https://doi.org/10.1111/j.1365-246X.2012.05546.x.

MacLaughlin, M., Sitar, N., Doolin, D., Abbot, T., 2001. Investigation of slope-stability kinematics using discontinuous deformation analysis. Int. J. Rock Mech. Min. Sci. 38, 753–762. https://doi.org/10.1016/S1365-1609(01)00038-7.

Matthews, A.J., Barclay, J., 2004. A thermodynamical model for rainfall-triggered volcanic dome collapse. Geophys. Res. Lett. 31. https://doi.org/10.1029/2003GL019310.

Matthews, A.J., Barclay, J., Carn, S., Thompson, G., Alexander, J., Herd, R., Williams, C., 2002. Rainfall-induced volcanic activity on Montserrat. Geophys. Res. Lett. 29. https://doi.org/10.1029/2002GL014863, 22-1-22–4.

Miller, C.A., Christenson, B.W., Byrdina, S., Vandemeulebrouck, J., Brakenrig, T., Britten, K., Shanks, J., Epstein, G., 2020. Snapshot of a magmatic/hydrothermal system from electrical resistivity tomography and fumarolic composition, Whakaari/White Island, New Zealand. J. Volcanol. Geotherm. Res. 400, 106909. https://doi.org/10.1016/j.jvolgeores.2020.106909.

Mordensky, S.P., Villeneuve, M.C., Kennedy, B.M., Heap, M.J., Gravley, D.M., Farquharson, J.I., Reuschlé, T., 2018. Physical and mechanical property relationships of a shallow intrusion and volcanic host rock, Pinnacle Ridge, Mt. Ruapehu, New Zealand. J. Volcanol. Geotherm. Res. 359, 1–20. https://doi.org/10.1016/j.jvolgeores.2018.05.020.

Moretti, L., Allstadt, K., Mangeney, A., Capdeville, Y., Stutzmann, E., Bouchut, F., 2015. Numerical modeling of the Mount Meager landslide constrained by its force history derived from seismic data. J. Geophys. Res. Solid Earth 120, 2579–2599. https://doi.org/10.1002/2014JB011426.

Moretti, R., Komorowski, J.-C., Ucciani, G., Moune, S., Jessop, D., de Chabalier, J.-B., Beauducel, F., Bonifacie, M., Burtin, A., Vallée, M., Deroussi, S., Robert, V., Gibert, D., Didier, T., Kitou, T., Feuillet, N., Allard, P., Tamburello, G., Shreve, T., Saurel, J.-M., Lemarchand, A., Rosas-Carbajal, M., Agrinier, P., Le Friant, A., Chaussidon, M., 2020. The 2018 unrest phase at La Soufrière de Guadeloupe (French West Indies) andesitic volcano: Scrutiny of a failed but prodromal phreatic eruption. J. Volcanol. Geotherm. Res. 393, 106769. https://doi.org/10.1016/j.jvolgeores.2020.106769.

Mueller, S.B., Varley, N.R., Kueppers, U., Lesage, P., Reyes Davila, G.Á., Dingwell, D.B., 2013. Quantification of magma ascent rate through rockfall monitoring at the growing/collapsing lava dome of Volcán de Colima, Mexico. Solid Earth 4, 201–213. https://doi.org/10.5194/se-4-201-2013.

Myers, A.J., Harnett, C.E., Holohan, E.P., Ryan, J.G., Zorn, E.U., Walter, T.R., Heap, M.J., 2024. Effects of cohesion and viscosity on lava dome growth following repose. J. Volcanol. Geotherm. Res. 455, 108196.

Nicollin, F., Gibert, D., Beauducel, F., Boudon, G., Komorowski, J.-C., 2006. Electrical tomography of La Soufrière of Guadeloupe Volcano: field experiments, 1D inversion and qualitative interpretation. Earth Planet. Sci. Lett. 244, 709–724. https://doi.org/10.1016/j.epsl.2006.02.020.

Ogburn, S.E., Loughlin, S.C., Calder, E.S., 2015. The association of lava dome growth with major explosive activity (VEI ≥ 4): DomeHaz, a global dataset. Bull. Volcanol. 77, 40. https://doi.org/10.1007/s00445-015-0919-x.

Opfergelt, S., Delmelle, P., Boivin, P., Delvaux, B., 2006. The 1998 debris avalanche at Casita volcano, Nicaragua: investigation of the role of hydrothermal smectite in promoting slope instability. Geophys. Res. Lett. 33. https://doi.org/10.1029/2006GL026661.

Peruzzetto, M., Komorowski, J.-C., Le Friant, A., Rosas-Carbajal, M., Mangeney, A., Legendre, Y., 2019. Modeling of partial dome collapse of La Soufrière of Guadeloupe volcano: implications for hazard assessment and monitoring. Sci. Rep. 9, 13105. https://doi.org/10.1038/s41598-019-49507-0.

Pirajno, F., 2009. Hydrothermal processes and wall rock alteration. In: Pirajno, F. (Ed.), Hydrothermal Processes and Mineral Systems. Springer, Netherlands, Dordrecht, pp. 73–164. https://doi.org/10.1007/978-1-4020-8613-7_2.

Poganj, A., Heap, M.J., Baud, P., 2025. Spatial distribution of alteration and strength in a lava dome: Implications for large-scale volcano stability modelling. J. Volcanol. Geotherm. Res. 463, 108344. https://doi.org/10.1016/j.jvolgeores.2025.108344.

Qi, Y., Wu, Y., 2022. Electrical conductivity of clayey rocks and soils: a non-linear model. Geophys. Res. Lett. 49, e2021GL097408. https://doi.org/10.1029/2021GL097408.

Reid, M.E., 2004. Massive collapse of volcano edifices triggered by hydrothermal pressurization. Geology 32, 373–376. https://doi.org/10.1130/G20300.1.

Reid, M.E., Sisson, T.W., Brien, D.L., 2001. Volcano collapse promoted by hydrothermal alteration and edifice shape, Mount Rainier, Washington. Geology 29, 779–782. https://doi.org/10.1130/0091-7613(2001)029<0779:VCPBHA>2.0.CO;2.

Rosas-Carbajal, M., Komorowski, J.-C., Nicollin, F., Gibert, D., 2016. Volcano electrical tomography unveils edifice collapse hazard linked to hydrothermal system structure and dynamics. Sci. Rep. 6, 29899. https://doi.org/10.1038/srep29899.

Rosas-Carbajal, M., Jourde, K., Marteau, J., Deroussi, S., Komorowski, J.-C., Gibert, D., 2017. Three-dimensional density structure of La Soufrière de Guadeloupe lava dome from simultaneous muon radiographies and gravity data. Geophys. Res. Lett. 44, 6743–6751. https://doi.org/10.1002/2017GL074285.

Salaün, A., Villemant, B., Gérard, M., Komorowski, J.-C., Michel, A., 2011. Hydrothermal alteration in andesitic volcanoes: trace element redistribution in active and ancient hydrothermal systems of Guadeloupe (Lesser Antilles). J. Geochem. Explor. 111, 59–83. https://doi.org/10.1016/j.gexplo.2011.06.004.

Schöpfer, M.P.J., Childs, C., Walsh, J.J., 2006. Localisation of normal faults in multilayer sequences. J. Struct. Geol. 28, 816–833. https://doi.org/10.1016/j.jsg.2006.02.003.

Schöpfer, M.P.J., Childs, C., Walsh, J.J., 2007. Two-dimensional distinct element modeling of the structure and growth of normal faults in multilayer sequences: 2. Impact of confining pressure and strength contrast on fault zone geometry and growth. J. Geophys. Res. Solid Earth 112. https://doi.org/10.1029/2006JB004903.

Sheldrake, T.E., Sparks, R.S.J., Cashman, K.V., Wadge, G., Aspinall, W.P., 2016. Similarities and differences in the historical records of lava dome-building volcanoes: implications for understanding magmatic processes and eruption forecasting. Earth Sci. Rev. 160, 240–263. https://doi.org/10.1016/j.earscirev.2016.07.013.

Siebert, L., 1984. Large volcanic debris avalanches: characteristics of source areas, deposits, and associated eruptions. J. Volcanol. Geotherm. Res. 22, 163–197. https://doi.org/10.1016/0377-0273(84)90002-7.

Siebert, L., Glicken, H., Ui, T., 1987. Volcanic hazards from Bezymianny- and Bandai-type eruptions. Bull. Volcanol. 49, 435–459. https://doi.org/10.1007/BF01046635.

Siebert, L., Simkin, T., Kimberly, P., 2010. Volcanoes of the World, Third edition. University of California Press.

Tang, C., 1997. Numerical simulation of progressive rock failure and associated seismicity. Int. J. Rock Mech. Min. Sci. 34, 249–261. https://doi.org/10.1016/S0148-9062(96)00039-3.

Tang, C., Tang, S., 2011. Applications of rock failure process analysis (RFPA) method. J. Rock Mech. Geotech. Eng. 3, 352–372. https://doi.org/10.3724/SP.J.1235.2011.00352.

Tost, M., Cronin, S.J., Procter, J.N., 2014. Transport and emplacement mechanisms of channelised long-runout debris avalanches, Ruapehu volcano, New Zealand. Bull. Volcanol. 76, 881. https://doi.org/10.1007/s00445-014-0881-z.

Ui, T., Matsuwo, N., Sumita, M., Fujinawa, A., 1999. Generation of block and ash flows during the 1990–1995 eruption of Unzen Volcano, Japan. J. Volcanol. Geotherm. Res. 89, 123–137. https://doi.org/10.1016/S0377-0273(98)00128-0.

Vallance, J.W., Schneider, D.J., Schilling, S.P., 2008. Growth of the 2004-2006 lava-dome complex at Mount St. Helens, Washington (no. 1750–9). In: Professional Paper. U.S. Geological Survey. https://doi.org/10.3133/pp17509.

Villemant, B., Hammouya, G., Michel, A., Semet, M.P., Komorowski, J.-C., Boudon, G., Cheminée, J.-L., 2005. The memory of volcanic waters: shallow magma degassing revealed by halogen monitoring in thermal springs of La Soufrière volcano (Guadeloupe, Lesser Antilles). Earth Planet. Sci. Lett. 237, 710–728. https://doi.org/10.1016/j.epsl.2005.05.013.

Villemant, B., Komorowski, J.C., Dessert, C., Michel, A., Crispi, O., Hammouya, G., Beauducel, F., De Chabalier, J.B., 2014. Evidence for a new shallow magma intrusion at La Soufrière of Guadeloupe (Lesser Antilles): insights from long-term geochemical monitoring of halogen-rich hydrothermal fluids. J. Volcanol. Geotherm. Res. 285, 247–277. https://doi.org/10.1016/j.jvolgeores.2014.08.002.

Voight, B., Elsworth, D., 2000. Instability and collapse of hazardous gas-pressurized lava domes. Geophys. Res. Lett. 27, 1–4. https://doi.org/10.1029/1999GL008389.

Wallace, C.S., Schaefer, L.N., Villeneuve, M.C., 2022. Material properties and triggering mechanisms of an andesitic Lava Dome Collapse at Shiveluch Volcano, Kamchatka, Russia, Revealed using the Finite Element Method. Rock Mech. Rock. Eng. 55, 2711–2728. https://doi.org/10.1007/s00603-021-02513-z.

Walter, T.R., Haghshenas Haghighi, M., Schneider, F.M., Coppola, D., Motagh, M., Saul, J., Babeyko, A., Dahm, T., Troll, V.R., Tilmann, F., Heimann, S., Valade, S., Triyono, R., Khomarudin, R., Kartadinata, N., Laiolo, M., Massimetti, F., Gaebler, P., 2019a. Complex hazard cascade culminating in the Anak Krakatau sector collapse. Nat. Commun. 10, 4339. https://doi.org/10.1038/s41467-019-12284-5.

Walter, T.R., Harnett, C.E., Varley, N., Bracamontes, D.V., Salzer, J., Zorn, E.U., Bretón, M., Arámbula, R., Thomas, M.E., 2019b. Imaging the 2013 explosive crater excavation and new dome formation at Volcán de Colima with TerraSAR-X, time-lapse cameras and modelling. J. Volcanol. Geotherm. Res. 369, 224–237. https://doi.org/10.1016/j.jvolgeores.2018.11.016.

Walter, T.R., Zorn, E.U., Harnett, C.E., Shevchenko, A.V., Belousov, A., Belousova, M., Vassileva, M.S., 2022. Influence of conduit and topography complexity on spine extrusion at Shiveluch volcano, Kamchatka. Commun. Earth Environ. 3, 1–10. https://doi.org/10.1038/s43247-022-00491-w.

Waxman, M.H., Smits, L.J.M., 1968. Electrical conductivities in oil-bearing shaly sands. Soc. Pet. Eng. J. 8, 107–122. https://doi.org/10.2118/1863-A.

Wessel, P., Smith, W.H.F., 1996. A global, self-consistent, hierarchical, high-resolution shoreline database. J. Geophys. Res. Solid Earth 101, 8741–8743. https://doi.org/10.1029/96JB00104.

Wessel, P., Luis, J.F., Uieda, L., Scharroo, R., Wobbe, F., Smith, W.H.F., Tian, D., 2019. The generic mapping tools version 6. Geochem. Geophys. Geosyst. 20, 5556–5564. https://doi.org/10.1029/2019GC008515.

Wong, T., Wong, R.H.C., Chau, K.T., Tang, C.A., 2006. Microcrack statistics, Weibull distribution and micromechanical modeling of compressive failure in rock. Mech. Mater. 38, 664–681. https://doi.org/10.1016/j.mechmat.2005.12.002.

Wu, C., Wang, Z.Z., Goh, S.H., Zhang, W., 2024. Comparing 2D and 3D slope stability in spatially variable soils using random finite-element method. Comput. Geotech. 170, 106324. https://doi.org/10.1016/j.compgeo.2024.106324.

Yu, X., Xu, T., Heap, M.J., Heng, Z., Ranjith, P.G., Su, B., Wasantha, P.L.P., Sun, G., 2023. Time-dependent virtual crack model of rock with application to slope stability. Eng. Anal. Bound. Elem. 154, 172–185. https://doi.org/10.1016/j.enganabound.2023.05.043.

Zhang, L.L., Fredlund, M.D., Fredlund, D.G., Lu, H., Wilson, G.W., 2015. The influence of the unsaturated soil zone on 2-D and 3-D slope stability analyses. Eng. Geol. 193, 374–383. https://doi.org/10.1016/j.enggeo.2015.05.011.

Zhang, C., Bai, Q., Han, P., Wang, L., Wang, X., Wang, F., 2023. Strength weakening and its micromechanism in water–rock interaction, a short review in laboratory tests. Int. J. Coal Sci. Technol. 10, 10. https://doi.org/10.1007/s40789-023-00569-6.

Zimbelman, D.R., Watters, R.J., Firth, I.R., Breit, G.N., Carrasco-Nunez, G., 2004. Stratovolcano stability assessment methods and results from Citlaltépetl, Mexico. Bull. Volcanol. 66, 66–79. https://doi.org/10.1007/s00445-003-0296-8.

Zorn, E.U., Le Corvec, N., Varley, N.R., Salzer, J.T., Walter, T.R., Navarro-Ochoa, C., Vargas-Bracamontes, D.M., Thiele, S.T., Arámbula Mendoza, R., 2019. Load stress controls on directional Lava Dome growth at Volcán de Colima, Mexico. Front. Earth Sci. 7. https://doi.org/10.3389/feart.2019.00084.